Computers and Geotechnics 171 (2024) 106343

Contents lists available at ScienceDirect

Computers and Geotechnics

journal homepage: www.elsevier.com/locate/compgeo

Research paper

Localization patterns emerging in CPTu tests in a saturated natural clay soil ☆

Kateryna Oliynyk [a,b], Matteo O. Ciantia [a,c], Claudio Tamagnini [b,*]

[a] University of Dundee, Dundee, United Kingdom
[b] Università degli Studi di Perugia, Perugia, Italy
[c] Università degli Studi di Milano Bicocca, Milan, Italy

ARTICLE INFO

Keywords:
CPTu tests
Natural clay soils
Strain localization
Nonlocal plasticity
Finite deformations
PFEM

ABSTRACT

In this work, the mechanics of cone penetration during CPTu tests in Osaka clay, a natural structured silty clay, was investigated with the Particle Finite Element Method (PFEM). To describe the behavior of the soil, the FD_Milan model, recently proposed by the Authors, was adopted. The model, based on the multiplicative decomposition of the deformation gradient, incorporates a scalar internal variable, the bond strength P_t, to quantify the effects of structure. The macroscopic description of mechanical destructuration effects is provided by the hardening law of P_t, according to which the bond strength decreases monotonically with accumulated plastic deformations. The brittle behavior resulting from the softening process associated to destructuration make the soil quite susceptible to the spontaneous development of strain localization in the form of shear bands. In order to deal with strain localization phenomena, the model is equipped with a non-local version of the hardening laws, incorporating a material constant – the characteristic length ℓ_c – which provides the material with an internal length scale. The objective of this work was to get some insight on the effects of the characteristic length and of the initial degree of structure on: the kinematics of the soil deformation around the advancing cone tip; the evolution of soil structure with accumulated plastic deformations; the excess pore pressure field generated in the soil as a result of the hydro-mechanical coupling between the solid skeleton and the pore water, and the net cone resistance measured at the base of the cone. The results of the PFEM simulations show that the deformations around the piezocone are strongly affected by the characteristic length. For heavily structured soils, when ℓ_c is relatively small with respect to cone radius, the accumulated plastic deviatoric deformation field is characterized by clearly visible shear bands while, as ℓ_c increases, the detection of localized deformation regions becomes more difficult, if not impossible. This depends on the fact that, for large values of ℓ_c, the shear band width may be of comparable size to the cone radius. In all cases, the soil around the advancing piezocone is subjected to a very strong destructuration process, which leads to the complete loss of bond strength in a large region around the cone tip and shaft. As a consequence, the use of conventional N_c values from the literature in the interpretation of the CPTu test performed in heavily structured soils could provide undrained strength values closer to the ultimate undrained shear strength. At the same time, the use of empirical correlation to estimate the yield stress in oedometric conditions would lead to a significant underestimation of the overconsolidation ratio.

1. Introduction

Recent development in particle-based numerical methods such as the Smoothed Particle Hydrodynamics (SPH, see, *e.g.*, Bui et al., 2008; Pastor et al., 2009, 2015; An et al., 2016), the Material Point Method (MPM, see, *e.g.*, Beuth and Vermeer, 2013; Abe et al., 2014; Bisht and Salgado, 2018) and the Particle Finite Element Method (PFEM, see, *e.g.*, Oliver et al., 2007; Carbonell et al., 2013; Monforte et al., 2017b, 2019) have allowed to address in a rational, accurate and efficient way the interpretation of the complex coupled deformation and flow processes which occur in a saturated soil mass undergoing extreme deformations, involving significant modifications in the configurations of the soil body with time, see for example the special issue of Acta Geotechnica dedicated to "Point-based methods and their applications in geomechanics" (Wu and Bui, 2021).

Among such problems, much interest has been drawn by the modeling of the so-called insertion processes, which are of relevance in a number of practical geomechanical applications, such as, for example, in-situ testing, soil sampling and pile driving. In particular, significant

☆ The authors dedicate this paper to the late Professor Patrick Selvadurai.

* Corresponding author.
E-mail address: claudio.tamagnini@unipg.it (C. Tamagnini).

https://doi.org/10.1016/j.compgeo.2024.106343

Available online 24 April 2024

attention has been devoted to the analysis of cone penetration tests, performed either with a standard penetrometer (CPT tests) or with piezocones with pore pressure transducers located at the base of the cone or at cone mid-height (CPTu tests). In fact, for their simplicity, reliability and relatively low cost, CPT and CPTu tests are widely used investigation tools for the characterization of both coarse- and fine-grained soils.

In geotechnical practice, the interpretation of CPT and CPTu tests is typically based on empirical and semi-empirical correlations, based on very crude descriptions of soil behavior (*e.g.*, the total stress approach with Tresca or von Mises models). Particle-based methods have been used to get valuable insight on the mechanics of the cone penetration process in both coarse-grained soils (Martinelli and Galavi, 2021; Martinelli and Pisanò, 2022; Moshfeghi et al., 2024) and fine-grained soils (Ceccato et al., 2016; Ceccato and Simonini, 2017; Monforte et al., 2018a,b, 2021; Zhang et al., 2021; Ciantia et al., 2022), often adopting fully coupled formulations capable of describing the pore pressure build-up around the advancing cone tip in low-permeability soils. Recently, Yost et al. (2022) and Boschi et al. (2024) used the MPM and PFEM to investigate the effects of embedded thin soil layers with different grain size distribution than the host soil. However, among the large number of contributions which can be found in the literature on this subject, only a few appear to have addressed the effects that cone penetration may induce in structured natural clays (see, *e.g.*, Hauser and Schweiger, 2021; Ciantia et al., 2022; Oliynyk et al., 2023).

As observed by Burland (1990), the peculiar fabric and the presence of interparticle bonds of various origin – collectively termed "structure" – affect the mechanical response of both soft and stiff natural clays by producing a net increase in shear strength and yield stress in one-dimensional compression, as well as the development of a non-negligible tensile strength. At the same time, structured soils are typically characterized by quite marked yield phenomena which, in deviatoric loading paths, are accompanied by a brittle behavior at failure, with a significant reduction of the shear strength with increasing deviatoric deformations. This is the consequence of the progressive degradation of the interparticle bonds ("destructuration") as the soil deformation increases.

The particular features of the response of structured clays may have two important effects on both the mechanics and the numerics of the piezocone penetration problem. First, the brittle nature of these materials make them quite susceptible to the spontaneous development of strain localization in the form of shear bands (Vardoulakis and Sulem, 1995; Borja, 2013). Second, the progressive reduction of the soil shear strength due to the destructuration process may affect significantly the mean total stress at the base of the cone – the cone resistance q_c – which is one of the measured quantities during the test, and from which the soil properties are determined.

The occurrence of localization has far-reaching consequences in the numerical modeling of inelastic deformation phenomena using classical elastoplasticity, which does not provide the material with an internal length scale. When strain localization occurs, the results of numerical simulations with the FE method, or any other displacement-based approach related to it, show a pathological dependence on the adopted spatial discretization in the post-localization regime (see, *e.g.*, Bažant et al., 1984; Bažant and Pijaudier-Cabot, 1988; de Borst, 1989). In fact, as the thickness of the localized zone tends to zero, the best resolution of the localized zone which can be provided by the adopted mesh is represented by a narrow zone spanning over a single element width (see, *e.g.*, Borja et al., 2013).

In order to restore the objectivity of the numerical solutions in presence of localized deformations, two main strategies have been pursued in computational mechanics, with varying degree of success. The first approach consists in treating the localized deformation band as a displacement discontinuity, whose geometry evolves during the loading process and on which a specific constitutive equations for the interface between the two parts of the body separated by the discontinuity needs to be defined (see, *e.g.*, Armero and Callari, 1999; Regueiro and Borja, 2001; Borja and Aydin, 2004; Borja, 2004). The second approach involves the modification of the constitutive theory in order to introduce some form of "non-locality". This can be achieved by means of various kind of gradient plasticity models (Vardoulakis and Aifantis, 1991; de Borst and Mühlhaus, 1992; Zervos et al., 2001; Chambon et al., 2001, 2004) or through non-local plasticity models of the integral type (see, *e.g.*, Bažant and Lin, 1988; Bažant and Jirásek, 2002, and references therein).

Hauser and Schweiger (2021) and Ciantia et al. (2022) adopted a particular version of non-local regularization in their plasticity models, based on Galavi and Schweiger (2010). In this non-local formulation, the material is endowed with a characteristic length ℓ_c, which controls the shear band width (Oliynyk et al., 2022). In these works, the value of the characteristic length was chosen mainly to achieve mesh-independent and smooth results in the CPTu simulations, but no systematic study was carried out to evaluate the effects of the adopted value of ℓ_c on the strain field around the cone tip and on the conventional test results (cone resistance and excess pore pressure at the piezocone probe).

In this work, the geomechanics-oriented PFEM code GPFEM (Monforte et al., 2017a; Carbonell et al., 2022), developed as an application module of the Kratos Multiphysics computational environment (Mataix Ferrándiz et al., 2020), was used to extend the previous numerical investigations. In particular, the study was focused on the effects that the characteristic length may have on the deformation field around the advancing piezocone, on the soil destructuration, on the excess pore pressure and on the cone resistance, computed during the penetration process.

To focus the investigation on a realistic scenario, the choice was made to adopt for the soil the properties of a specific natural structured clay – the Osaka clay (Adachi et al., 1995) – selected as a typical example of this class of geomaterials. The FD_Milan model proposed by Oliynyk et al. (2021) was adopted to provide an accurate description of the main aspects of Osaka clay relevant for the problem at hand.

This model – which can be considered the extension to finite deformations of the isotropic hardening models for bonded geomaterials developed at the Technical University of Milan over the last two decades (Tamagnini et al., 2002; Nova et al., 2003; Tamagnini and Ciantia, 2016) – is based on the multiplicative decomposition of the deformation gradient and on the adoption of a suitable free energy function to describe the elastic response of the material. In addition, it features non-local hardening laws which provide the internal length scale necessary to obtain objective numerical results.

The outline of the remainder of the paper is as follows. In Sections 2 and 3 we summarize briefly the constitutive equations of the FD_Milan model and the basics of the PFEM method, to make the paper self-contained. Section 4 deals with the calibration of the model constants for Osaka clay, based on some conventional laboratory test results available in the literature. The details of the CPTu simulation program performed in this study are given in Section 5. Some selected PFEM results are presented and discussed in Section 6. Finally, Section 7 summarized the main conclusions obtained from this work.

Notation

In the following, all stresses and stress-related quantities are effective, unless otherwise stated. The sign convention of soil mechanics (compression positive) is adopted throughout, except where otherwise stated. Both direct and index notations are used to represent vector and tensor quantities according to convenience. In direct notation, vectors and second-order tensors are represented by boldface italic characters; upper- and lowercase blackboard bold fonts – as for example $\mathbb{C}^e$ and $\mathbb{e}^e$ – are used for fourth-order tensors. Following standard practice, for any two vectors $\boldsymbol{v}, \boldsymbol{w} \in \mathbb{R}^3$, the dot product is defined as: $\boldsymbol{v} \cdot \boldsymbol{w} := v_i w_i$, and the dyadic product as: $[\boldsymbol{v} \otimes \boldsymbol{w}]_{ij} := v_i w_j$. Accordingly, for any two

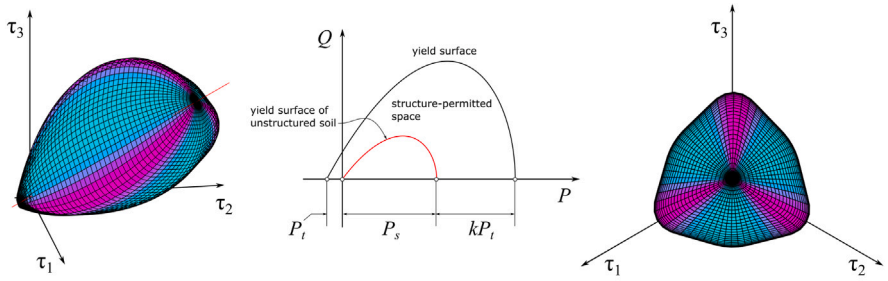

Fig. 1. Yield surface of the FD_Milan model: (a) three-dimensional view in the principal Kirchhoff stress space; (b) representation in Q: P plane of the Kirchhoff stress invariants, for $\theta = \pi/6$; (c) view in the direction of the isotropic axis.

second-order tensors $\boldsymbol{X}, \boldsymbol{Y} \in \mathbb{L}$, $\boldsymbol{X}\cdot\boldsymbol{Y} := X_{ij}Y_{ij}$ and $[\boldsymbol{X}\otimes\boldsymbol{Y}]_{ijkl} := X_{ij}Y_{kl}$. The quantity $\|\boldsymbol{X}\| := \sqrt{\boldsymbol{X}\cdot\boldsymbol{X}}$ denotes the Euclidean norm of the second order tensor $\boldsymbol{X}$.

In the representation of Cauchy and Kirchhoff stress tensors, $\boldsymbol{\sigma}$ and $\boldsymbol{\tau}$, use is made of the following invariant quantities:

$$p := \frac{1}{3}\,\mathrm{tr}(\boldsymbol{\sigma}) \qquad q := \sqrt{\frac{3}{2}}\,\|\boldsymbol{s}\| \qquad S := \sin(3\theta) = \sqrt{6}\frac{\mathrm{tr}(\boldsymbol{s}^3)}{[\mathrm{tr}(\boldsymbol{s}^2)]^{3/2}}$$

$$P := \frac{1}{3}\,\mathrm{tr}(\boldsymbol{\tau}) \qquad Q := \sqrt{\frac{3}{2}}\,\|\boldsymbol{s}_\tau\| \qquad S := \sin(3\theta) = \sqrt{6}\frac{\mathrm{tr}(\boldsymbol{s}_\tau^3)}{[\mathrm{tr}(\boldsymbol{s}_\tau^2)]^{3/2}}$$

where: $\boldsymbol{s} := \boldsymbol{\sigma} - p\mathbf{1}$ is the deviatoric part of $\boldsymbol{\sigma}$; $\boldsymbol{s}_\tau := \boldsymbol{\tau} - P\mathbf{1}$ is the deviatoric part of $\boldsymbol{\tau}$; $\boldsymbol{s}^2$ and $\boldsymbol{s}^3$ are the square and the cube of $\boldsymbol{s}$; $\boldsymbol{s}_\tau^2$ and $\boldsymbol{s}_\tau^3$ are the square and the cube of $\boldsymbol{s}_\tau$, and θ is the Lode angle.

2. Finite deformation modeling of natural structured clays: the FD_Milan model

To represent the mechanical response of natural, structured clay soils in finite deformation kinematics, the FD_Milan model developed by Oliynyk et al. (2021) was adopted in this work.

The FD_Milan model is a non-associative, three-invariant isotropic hardening finite-deformation plasticity model for structured soils and weak rocks, based on the multiplicative decomposition of the deformation gradient and on the adoption of a suitable free energy function to describe the elastic response of the material.

The details of the constitutive equations of the model are summarized in Appendix A. The model is equipped with two scalar internal variables, the preconsolidation pressure P_s, which accounts for the hardening/softening effects due to volumetric and deviatoric plastic strains, and the bond strength P_t, which quantifies, from a macroscopic point of view, the effects of material fabric and interparticle bonding. The representation of the yield surface in the Kirchhoff principal stress space and in the Kirchhoff stress invariants plane Q: P, is provided in Fig. 1.

Fig. 1b allows to highlight the role played by the preconsolidation pressure P_s and the bond strength P_t in controlling the size of the elastic domain. The bond strength accounts for a net increase of the isotropic yield stress in compression (by a quantity kP_t, with k a material constant) as compared to the unstructured soil, and for the development of a true tensile strength, quantified by the intercept of the yield surface with the positive P axis at $P = -P_t$.

In order to provide a characteristic length scale to the constitutive equation, with the objective of regularizing the numerical solution in presence of strain localization, the integral non-local approach of Bažant et al. (1984) was adopted, in which the internal variables are treated as non-local, spatially averaged quantities over a neighborhood Ω of the material point, see Appendix B. The size of this neighborhood is controlled by a material constant, ℓ_c, known as characteristic length.

As shown in Appendices A and B, the FD_Milan model is fully characterized by 17 material constants with a clear role in controlling the different features of the constitutive equations. These constants are summarized in Table 1. The first group of constants ($\hat{\kappa}$, G_0, α and P_r) define the hyperelastic behavior of the material. The shapes of the yield function f and of the plastic potential g are controlled by the second and third groups of constants ($M_{f,c}$, α_f, μ_f and $M_{g,c}$, α_g, μ_g). The constants controlling the evolution of the internal variables P_s and P_t with plastic deformations are provided by the fourth group. Finally, the quantities k_h and ℓ_c represent the hydraulic permeability and the characteristic length of the material.

Table 1
Sets of material constants adopted in the PFEM simulations.

		Set #1	Set #2	Note
$\hat{\kappa}$	(–)	0.03	0.03	Elastic constants
G_0	(kPa)	3000.0	3000.0	
α	(–)	0.0	0.0	
P_r	(kPa)	60.0	60.0	
$M_{f,c}$	(–)	1.1	1.1	Yield function constants
α_f	(–)	0.75	0.75	
μ_f	(–)	1.5	1.5	
$M_{g,c}$	(–)	1.1	1.1	Plastic potential constants
α_g	(–)	0.75	0.75	
μ_g	(–)	1.5	1.5	
ρ_s	(–)	12.5	12.5	Hardening rules constants
ρ_t	(–)	5.0	5.0	
ξ_s	(–)	0.0	0.0	
ξ_t	(–)	1.0	2.0	
k	(–)	5.0	5.0	
k_h	(m^2/s/kPa)	1.0e−8	1.0e−8	Hydraulic conductivity
ℓ_c	(m)	Variable	Variable	Characteristic length

3. Outline of GPFEM

In the application of GPFEM to fully saturated soils, the balance equations of mass and (quasi-static) linear momentum are cast in an updated Lagrangian description, *i.e.*, all variables are assumed to be known in the current configuration at time t. A domain discretization is required in order to solve the governing equations with the standard FE method. As the quality of the numerical solution depends on the chosen spatial discretization, in PFEM the mesh is refined by performing a re-triangulation of the domain when needed, typically in regions with high deformation gradients.

Central to the method is the possibility of performing very efficient mesh re-triangulation and refinement using h — adaptive techniques based on extended Delaunay tessellation and mesh smoothing. Low order elements – linear triangles in 2d and linear tetrahedra in 3d – are used in GPFEM due to their simplicity and low computational cost. To avoid locking problems typical of low-order elements and instabilities associated to the equal order of approximation for both displacement and pore pressure fields, the mixed $\boldsymbol{u}-\Theta-p_w$ formulation

Table 2
Physical and index properties of Eastern Osaka clay.
Source: Data from Adachi et al. (1995).

Specific solid density γ_s/γ_w	2.67–2.703
Natural water content w_0	65%–72%
Liquid limit w_L	69.2–75.1%
Plastic limit w_P	24.5–27.3%
Plasticity index I_p	41.9–50.6%
Activity A	0.54
Clay fraction	44%
Silt fraction	49%
Sand fraction	7%

of Monforte et al. (2017b) for coupled deformation and flow problems in porous media is adopted. In the formulation of the relevant balance equations, a stabilization term is added to the weak form of the volumetric deformation balance equation, according to the Polynomial Pressure Projection (PPP) method (Dohrmann and Bochev, 2004), while the Fluid Pressure Laplacian stabilization technique (FPL, Truty and Zimmermann, 2006) is used to address the stability problems associated to the failure to meet the Inf-Sup conditions of standard linear triangles or tetrahedra with equal order of approximation for displacements and pore water pressures.

4. Calibration of the model for a natural soil: the Osaka clay

4.1. Main characteristics of Osaka clay

For the present study, Eastern Osaka clay, studied by Adachi et al. (1995) and reported in this work simply as "Osaka clay", was chosen as a representative soft natural fine-grained soil displaying the typical behavior of structured clays. Osaka clay is a natural Pleistocene silt with clay deposit with a thickness varying between 15 and 20 m, found in Tsurumi, East Osaka. The main physical and index properties of the soil are summarized in Table 2.

During its geological history, Osaka clay has undergone a cation leaching process, which resulted in the substitution of part of the sodium (Na^+) ions with hydrogen (H^+). This process is responsible for its significant sensitivity, quantified by an S_t value of about 10, as measured in laboratory vane tests. The observed sensitivity can be interpreted as a manifestation of the presence of structure in the natural soil, which is confirmed by the experimental evidence obtained from both oedometric tests (*e.g.*, post-yield compression curve displaying an initial high compressibility, which reduces with increasing volumetric deformations) and undrained triaxial compression tests (*e.g.*, brittle behavior at failure during the deviatoric compression stage), see, *e.g.*, Leroueil and Vaughan (1990).

4.2. Experimental results used in the calibration

A large experimental investigation campaign was conducted on Eastern Osaka clay for the construction of a subway tunnel in the Tsurumi district, as reported in detail by Adachi et al. (1995). Undisturbed, high-quality block and tube samples of the clay were used to perform a wide spectrum of laboratory test, including triaxial unconfined compression (TX-UU) tests, oedometric (OED) tests, isotropically (I) and anisotropically (A) consolidated triaxial compression (TX-C) and extension (TX-E) undrained (U) tests.

For the purposes of the present work, the calibration of the FD_Milan model was carried out considering the limited set of laboratory tests reported in Table 3. In particular, our interest was focused on: (a) oedometric compression tests on both natural and reconstituted samples, to quantify the initial level of soil structure and its evolution with accumulated plastic deformations along stress paths which do not lead the soil to shear failure; (b) undrained TX compression tests on isotropically consolidated specimens at two levels of initial mean effective stress; (c) undrained TX extension tests on isotropically consolidated specimens at two levels of initial mean effective stress. Given the isotropic nature of the constitutive model adopted in this study, in the calibration process we did not consider anisotropically consolidated TX test results, nor the results obtained from horizontally trimmed samples.

Table 3
Set of laboratory tests used for the calibration of the FD_Milan model.

Test ID	Test type	Soil state	p_0 (kPa)	e_0 (–)	p_{s0} (kPa)	p_{t0} (kPa)
–	OED	Natural	–	1.80	30.0	10.0
–	OED	Reconstituted	–	1.80	10.0	0.0
TS5–1	TX–CIU	Natural	78.4	1.85	20.0	10.0
TS5–4	TX–CIU	Natural	39.2	1.79	15.0	10.0
TS5–8	TX–EIU	Natural	78.4	1.73	20.0	10.0
TS5–9	TX–EIU	Natural	39.2	1.70	20.0	10.0

Since the experimental data used for the calibration were interpreted assuming homogeneous deformation of the specimen during the test, the available information does not allow to calibrate the characteristic length ℓ_c of the soil. Moreover, as the test interpretation was done without considering geometric non-linearity effects, the simulations of the test results were performed assuming infinitesimal deformations.

4.3. Determination of the elastic properties

The elastic compressibility coefficient $\hat{\kappa}$ was estimated from the results of the oedometric test performed on the reconstituted soil. In fact, this quantity can be related to the swelling coefficient C_s^*, measured as the slope of the unloading-reloading branch of the compressibility curve, via the relation $\hat{\kappa} \simeq 0.434\, C_s^*/(1+e_0)$. The value of $\hat{\kappa}$ thus obtained is reported in Table 1.

In lack of experimental evidence of elastic volumetric/deviatoric coupling, the coefficient α was set equal to zero. Under this assumption, the hyperelastic model is characterized by a constant shear modulus G_0 and by an apparent pressure-dependent bulk modulus K, provided by the following relation (see Oliynyk et al., 2021):

$$K = \begin{cases} \dfrac{p}{\hat{\kappa}} & \text{if } p \geq p_r \\ \dfrac{p_r}{\hat{\kappa}} & \text{otherwise} \end{cases} \tag{1}$$

According to Eq. (1), the bulk modulus is proportional to the mean Cauchy effective stress p, down to a lower threshold value set by p_r.

The shear modulus value G_0 was calibrated from the initial portion of the stress/strain curves of the tests TS5–1, TS5–4, TS5–8 and TS5–9, as:

$$G_0 = \frac{q}{3\epsilon_s} = \frac{q}{3\,|\epsilon_a|}$$

since in isochoric deformation processes $\epsilon_s = \epsilon_a$. The value of $G_0 = 3000$ kPa was found to provide a good match between model predictions and experimental data from both TX compression and extension tests, see Table 1.

Finally, the adopted value of the reference pressure p_r was chosen by assuming that the apparent Poisson's ratio ν_{app}, provided by the relation:

$$\nu_{\text{app}} := \frac{3K - 2G_0}{6K + 2G_0}$$

attains its minimum value $\nu_{\text{app}} = 0$ at the threshold $p = p_r$. The corresponding value of P_r, in terms of Kirchhoff mean stress (positive in compression), is listed in Table 1.

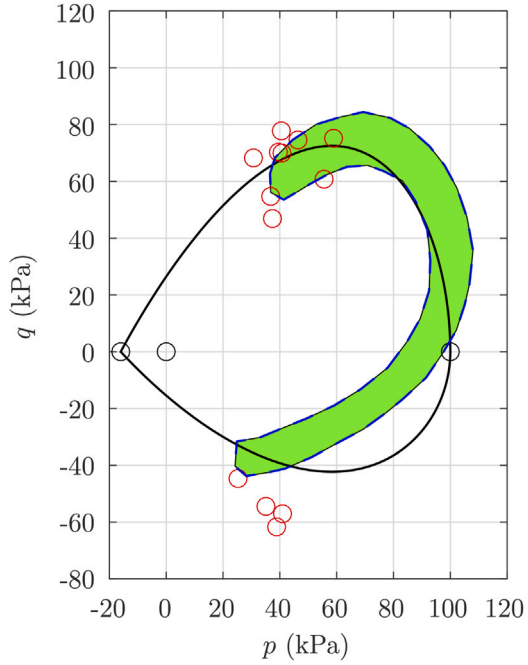

Fig. 2. Yield points obtained from isotropically consolidated triaxial compression and extension tests (red dots) and limit state surface identified by Adachi et al. (1995) (green area).

4.4. Determination of yield surface and plastic potential constants

In the work of Adachi et al. (1995), Fig. 20 report the collection of yield points observed in different testing conditions, as well as the region identified as "limit state surface". This data, reproduced in Fig. 2, was used as a starting point for the evaluation of the yield function constants $M_{f,c}$, α_f and μ_f.

The yield surface obtained with the values of these constants reported in Table 1, assuming $p_t = 16$ kPa, $p_s = 20$ kPa and $p_m = 80$ kPa, is plotted in Fig. 2 with a full black line. Note that, in the figure, the values of the (non-negative) deviatoric stress q for triaxial extension states are multiplied by $\sin(3\theta) = -1$, as done in Adachi et al. (1995) for a more clear representation of experimental data. Overall, the model yield surface appears to reproduce reasonably well the available experimental evidence. Due to the assumption of material isotropy, the yield surface cannot capture the slight rotation of Adachi et al. (1995) limit state surface, originated by the anisotropic compression experienced during the soil deposition. Also, the yield points determined from TX extension tests appear to overshoot the yield surface by a significant amount. However, as the mobilized friction angles computed at these yield states appear very large and quite unrealistic, there is reason to believe that the peak stress reached in TX extension tests are not fully reliable.

As for the plastic potential, in lack of accurate experimental data on either soil dilatancy or excess pore water pressure evolution with deviatoric strains during the shearing stages of the TX tests, we assumed that the plastic flow is associated, and therefore:

$$M_{g,c} = M_{f,c} \qquad \alpha_g = \alpha_f \qquad \mu_g = \mu_f$$

see Table 1.

4.5. Determination of the hardening constants

The constant ρ_s controls the evolution of the preconsolidation pressure P_s with accumulated plastic volumetric and deviatoric deformations. It can be related to the compressibility constants $\hat{\lambda}$ and $\hat{\kappa}$ of the reconstituted soil, measured in $\ln(1+e)$: $\ln(p)$ plane, by the relation:

$$\rho_s = \frac{1}{\hat{\lambda} - \hat{\kappa}}$$

The value of $\hat{\lambda}$ was estimated from the results of the oedometric test performed on the reconstituted soil, by the relation $\hat{\lambda} \simeq 0.434\, C_c^*/(1+e_0)$, where C_c^* is the virgin compression coefficient of the normally consolidated reconstituted soil in oedometric compression, as measured in e: $\log(\sigma_a)$ plots. The value of ρ_s thus obtained is reported in Table 1. In order to incorporate the concept of critical state for the completely destructured material, the internal variable P_s must be characterized by pure volumetric hardening. This is achieved by setting the constant ξ_s to zero.

The hardening constants controlling the destructuration process, ρ_t and ξ_t were calibrated by fitting the oedometric compressibility curve of the natural soil in the fully plastic regime, and the stress–strain curves of undrained TX compression tests performed at different initial mean effective stress on the natural soil. The shape of the oedometric compression curve of the natural soil, in the e: $\log(\sigma_a)$ plane, is mainly controlled by ρ_t. The constant ξ_t affects significantly the post-peak response observed in undrained TX tests, where deviatoric plastic deformations are prevailing over the plastic volumetric deformations. The values of ρ_t thus obtained is reported in Table 1. The two values of ξ_t identified in the calibration, which provide the lower and upper bounds to the observed response of the soil during the deviatoric compression stage, are reported in Table 1.

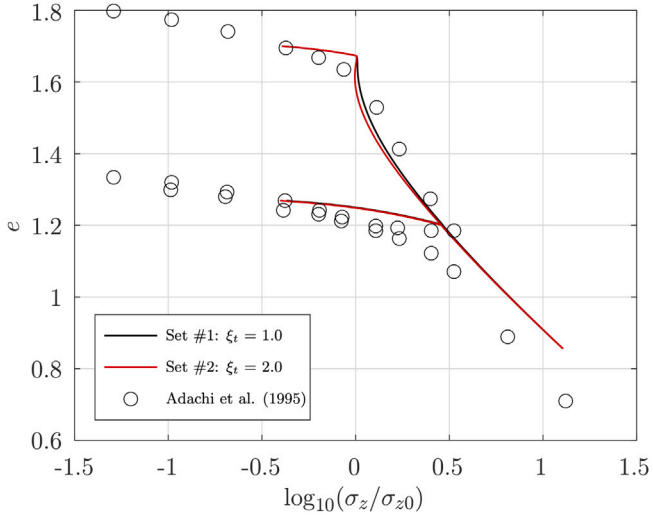

Fig. 3. Oedometric test on natural Eastern Osaka clay: comparison between experimental and predicted compression curves on the e: $\log_{10}(\sigma_z/\sigma_{z0})$, with σ_{z0} = 98 kPa.

4.6. Comparison between experimental data and model predictions

To assess the quality of the calibration process, the comparison between model predictions and the experimental data from the tests of Table 3 is shown in Figs. 3–7. The initial values of the internal variables, $P_{s0} = p_{s0}$ and $P_{t0} = p_{t0}$, were set as indicated in Table 3. All the simulations were performed with both sets of constants reported in Table 1.

Fig. 3 shows the comparison between the experimental and predicted compression curves in the e : $\log_{10}(\sigma_z/\sigma_{z0})$ obtained in the oedometric test performed on natural Osaka clay. The model predictions captures well the curved shape of the post-yield compression part of the test and the slope of the unloading–reloading curve. The discrepancy observed in the void ratio values between the experimental and the predicted virgin loading branch after the axial stress cycle is

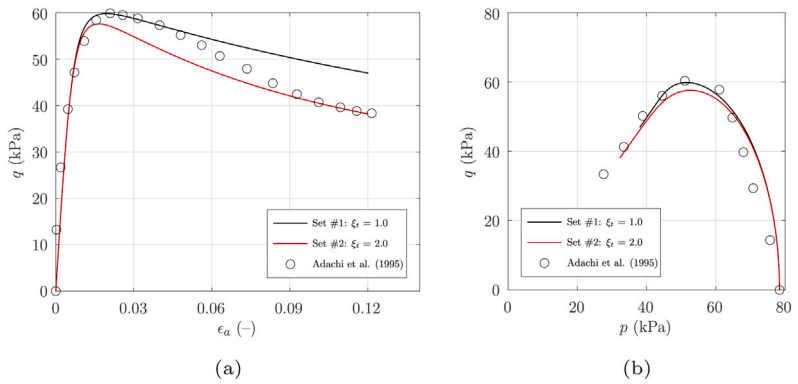

Fig. 4. Undrained triaxial compression test TS5–1 on natural Eastern Osaka clay: comparison between experimental data and predicted results in (a) q: ϵ_a plane, and (b) q: p plane.

the result of a permanent reduction of void ratio accumulated during the unloading–reloading path. This results in a downward shift of the virgin compression curve, which cannot be captured by the hyperelastic response of the model upon unloading–reloading. The comparison between the simulations performed with the two sets of constants indicates that the effect of ξ_t on the model response is relatively limited for this particular loading condition. This justifies *a posteriori* the assumption made in the calibration process that the shape of the oedometric compression curve is mainly controlled by ρ_t.

The results of the triaxial compression test TS5–1 on natural Eastern Osaka clay are plotted together with the model predictions in Fig. 4. In particular, Fig. 4(a) shows the measured and predicted stress–strain curves of the material in the q: ϵ_a plane, while the corresponding undrained stress paths are shown in Fig. 4(b) in the q: p plane. In test TS5–1, the mean effective stress at the beginning of the deviatoric loading stage is 78.4 kPa (see Table 3), very close to the isotropic yield stress. The material is therefore almost "normally consolidated". The response of the material in the undrained deviatoric loading stage is characterized by the development of positive excess pore water pressures, which cause the stress path to bend to the left as the deviatoric stress q increases. Differently from unstructured virgin soils, q does not attain its maximum value at large deformations upon reaching critical state conditions. Rather, a peak in q is observed at relatively small strains, followed by a reduction towards the final critical state conditions. This is the result of the progressive destructuration of the natural soil, mainly due to the accumulated plastic deviatoric deformations. The model captures this behavior accurately, both from a qualitative and a quantitative point of view. Under undrained shearing, plastic deviatoric strains are much larger than plastic volumetric strains; therefore the effects of the constant ξ_t on the model predictions are more significant than in the case of one-dimensional compression. The larger value of ξ_t seems to capture better the post-peak response of the soil. However, it must be observed that care must be exercised in considering the measurements done in the post-peak part of the test as an actual feature of the material response, since there is no guarantee that, in this regime, the stress and strain fields are not affected by the spontaneous formation of shear bands within the specimen (see, *e.g.*, Vardoulakis and Sulem, 1995).

The results of the triaxial compression test TS5–4 on natural Eastern Osaka clay are plotted together with the model predictions in Fig. 5, where Fig. 5(a) shows the measured and predicted stress–strain curves of the material in the q: ϵ_a plane, while the corresponding undrained stress paths are shown in Fig. 5(b) in the q: p plane. In this test, the mean effective stress at the beginning of the deviatoric loading stage is 39.2 kPa (see Table 3), which is slightly less than half the isotropic yield stress. This specimen can therefore be considered as slightly overconsolidated. As expected, the stress–strain response of the material is characterized by a peak deviatoric stress, reached at relatively small strains, followed by a softening response with a significant reduction of q towards the end of the test. This softening is accompanied by a significant increase in pore water pressure – see the descending branch of the stress path in Fig. 5(b) – which is the result of a clear tendency of the solid skeleton to develop contractant plastic volumetric deformations. Again, this is a consequence of the progressive destructuration taking place in the specimen during the deviatoric loading stage. The model captures well the observed behavior, both from a qualitative and a quantitative point of view.

The results of undrained triaxial extension tests TS5–8 (p_0 = 78.4 kPa) and TS5–9 (p_0 = 39.2 kPa) are compared with model predictions in Figs. 6 and 7, respectively. In the representation of the test results, the deviatoric stress q is assumed negative in extension, following the same convention discussed in the representation of the yield states in Fig. 2. The comparison between model prediction and experimental observations for test TS5–8 is relatively good until $\epsilon_a \simeq -0.01$, when the predicted stress–strain curves show a (negative) peak in q. After this axial strain level, the model predictions show – as expected – a slight reduction in the deviatoric stress caused by the progressive loss of structure of the material. The observed material response, however, is characterized by a monotonically decreasing evolution of q as ϵ_a decreases, with the peak (negative) deviatoric stress reached at very large strain levels. The same qualitative observations can be made for the comparison between model predictions and experimental observations for test TS5–9, for which the differences between the calculated and measured stress–strain curves and stress paths are even larger. This is certainly a consequence of some model limitations, in particular of the assumption of material isotropy. However, the observed discrepancy may be, at least in part, attributed to some inaccuracies in the experimental data which, for both extension tests, cannot be considered as fully reliable, for the following two main reasons. First, it appears unlikely that the destructuration process which should certainly have occurred in these tests did not result in the progressive reduction of the deviatoric stress and the mobilized friction angle as the axial deformations increased in absolute value. Second, the mobilized friction angles corresponding to the measured value of the q/p ratio at the end of both tests are unrealistically high, exceeding 55 degrees in both cases.

Considering all the results presented in this section, we can conclude that the calibration process leading to the two sets of material constants reported in Table 1 is satisfactory, and that both sets are capable of providing quantitatively good predictions of the behavior of Osaka clay, within the limits of the constitutive assumptions made in the development of the FD_Milan model. In the PFEM simulations described in the following Sections 5 and 6, the choice was made to adopt the set #2 of material constants to characterize the Osaka clay behavior because it captures slightly better the softening effects due to accumulated plastic deviatoric strains, which are expected to dominate the kinematics of soil deformation around the cone tip in almost undrained conditions.

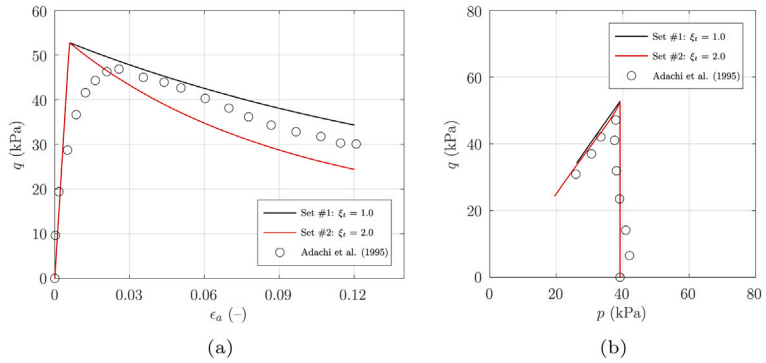

Fig. 5. Undrained triaxial compression test TS5–4 on natural Eastern Osaka clay: comparison between experimental data and predicted results in (a) q: ϵ_a plane, and (b) q: p plane.

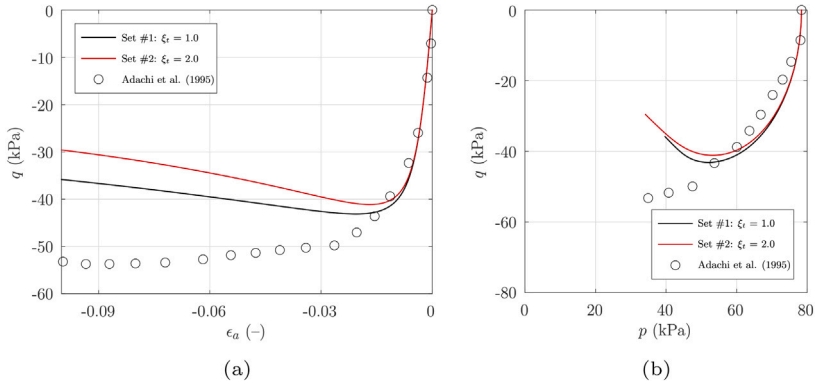

Fig. 6. Undrained triaxial extension test TS5–8 on natural Eastern Osaka clay: comparison between experimental data and predicted results in (a) q: ϵ_a plane, and (b) q: p plane.

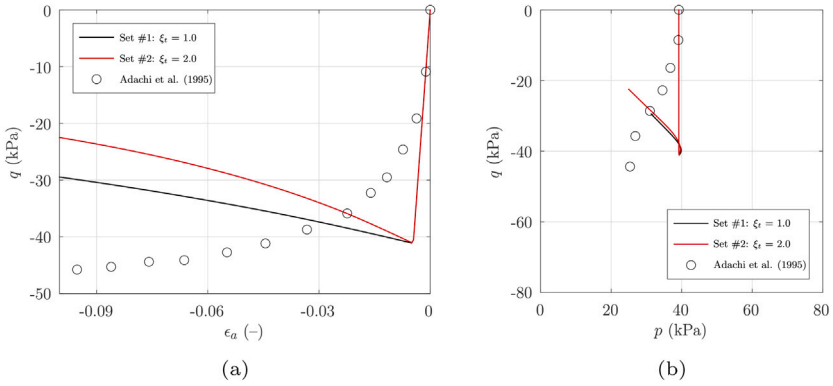

Fig. 7. Undrained triaxial extension test TS5–9 on natural Eastern Osaka clay: comparison between experimental data and predicted results in (a) q: ϵ_a plane, and (b) q: p plane.

5. PFEM simulations of CPTu tests

A series of PFEM simulations of CPTu tests in saturated Osaka clay – calibrated as discussed in the previous Section 4 – was performed to investigate the effects of the characteristic length, ℓ_c, adopted for the soil and of its initial bond strength, P_{t0}.

All the PFEM simulations were performed as fully coupled hydromechanical problems, adopting the mixed $\boldsymbol{u} - \Theta - p_w$ formulation of Monforte et al. (2019) and the set # 2 of material constants of Table 1.

The geometry of the problem is shown in Fig. 8. A standard piezocone, with radius R = 1.78 cm and a cone tip angle of 60° is inserted in a cylindrical calibration chamber, with radius B = 0.7 m and height H = 1.0 m, filled with fully saturated soil. In the PFEM simulations, the problem is modeled as axisymmetric.

In all the simulations, the piezocone is wished-in-place at an initial elevation z_0 = 0.0 m (0.1 m below the top surface of the soil layer) and then displaced downwards at a constant penetration speed of 2.0 cm/s, up to an elevation $z \simeq -20R$. At any penetration depth, the cone resistance q_c is computed as the ratio F_c/A_c between the resultant force acting at the base of the cone, F_c, and the cone base area, $A_c = \pi R^2$. The piezocone is equipped with two pore pressure probes, located as shown in Fig. 8, where the excess pore pressure Δu induced in the soil by the deformation process is calculated as the cone advances. The piezocone tip and its lateral surface are modeled as rigid, impervious surfaces, and a smooth contact interface with the soil is employed to simulate the piezocone-soil interaction. This assumption allows to increase significantly the computational efficiency in the simulations, and is supported by the observations made by Boschi et al. (2024), who report that the effect of cone-soil interface friction on the

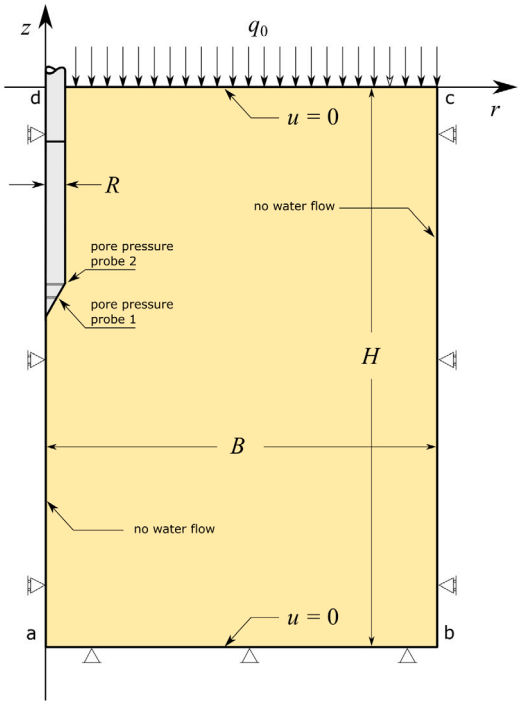

Fig. 8. Geometry of the CPTu test simulations with assumed boundary conditions.

computed value of the cone resistance are very small, for both coarse- and fine-grained soils.

Given the relatively small dimensions of the calibration chamber, the self weights of the pore water and of the soil was ignored and the initial pore water pressure was assumed uniform and equal to zero.

The boundary conditions adopted for the soil deformation and the pore water flow are summarized in Fig. 8. Zero horizontal displacements and water flow were assumed on the symmetry axis da. The bottom surface ab was considered as rigid and perfectly rough. The lateral surface bc was assumed as rigid and perfectly smooth. At the top surface of the soil body, cd, a constant and uniform normal pressure $q_0 = 100$ kPa was applied. A constant pore water pressure $u = 0$ was imposed at both the top and bottom surfaces, while the lateral surface was considered as impervious. Consistent with these boundary conditions, the initial Cauchy effective stress in the soil mass was assumed axisymmetric, with components $\sigma_z = 100$ kPa and $\sigma_r = K_0\sigma_z$, in which $K_0 = 0.6$. The initial value of the preconsolidation pressure P_{s0} was set to 120 kPa in all the simulations, while three different initial values were considered for the bond strength P_{t0}, see Table 4.

The complete program of the PFEM simulations is detailed in Table 4. The selected values of ℓ_c range from a relatively small fraction of the cone radius (14%), to a 3 times larger one (42%). The chosen values for P_{t0} provide a large range of different initial soil structures, going from strong ($P_{t0} = 60$ kPa) to medium ($P_{t0} = 30$ kPa) to weak ($P_{t0} = 5$ kPa), respectively. The simulations took CPU times ranging from about 20 to 79 h on a laptop computer with an AMD Ryzen 7 processor, depending on the assumed value of ℓ_c (which controls the final number of elements in the mesh) and on the number of CPUs used (2 or 4).

6. Discussion of results

6.1. Time evolution of selected field variables

The evolution of some selected field variables with space and time is presented in the following in the form of a series of contour maps evaluated at different time stations, namely $t = 5$, 9, 12 and 15 s, corresponding to normalized penetration depths $(z - z_0)/R$ equal to 5.62, 10.11, 13.48 and 16.85, respectively.[1]

Table 4
Program of PFEM simulations of CPTu tests on Osaka clay.

Test #	ℓ_c/R (–)	P_{s0} (kPa)	P_{t0} (kPa)
r102	0.14	120.0	60.0
r103	0.14	120.0	30.0
r104	0.14	120.0	5.0
r202	0.28	120.0	60.0
r203	0.28	120.0	30.0
r204	0.28	120.0	5.0
r302	0.42	120.0	60.0
r303	0.42	120.0	30.0
r304	0.42	120.0	5.0

Accumulated plastic deviatoric deformation

The contour maps of the accumulated plastic deviatoric deformation, E_s^p, are shown in Figs. 9 and 10 for some selected simulations. The first figure refers to the results of simulations r102 and r302, performed with the same initial bond strength ($P_{t0} = 60$ kPa) and the two extreme values of the normalized characteristic length ($\ell_c/R = 0.14$ and 0.42, respectively). The second figure refers to the results of simulations r102 and r104, performed with the same value of the normalized characteristic length ($\ell_c/R = 0.14$) and the two extreme values of the initial bond strength ($P_{t0} = 60$ and 5 kPa, respectively).

By looking at the results on the top row of Fig. 9, it can be noted that the plastic deviatoric strain field is characterized by clearly visible localization zones, in the form of shear bands, which originate in correspondence of the piezocone sleeve and then propagate downwards until they reach the cone axis well below the cone tip. As the cone advances, the zone of soil between the tip and the shear band is deformed until the shear band is incorporated within this region and disappears. At the same time, a new shear band is initiated at the cone flank and the localized deformation mechanisms is replicated again over and over. It is worth noting that, in this case, the evolution of the deviatoric deformation field is not stationary around the advancing cone tip, as it is assumed in some CPTu modeling approaches based on the theory of cavity expansion (Salgado et al., 1997; Salgado and Prezzi, 2007; Suzuki and Lehane, 2015) or on the Strain Path Method (Baligh, 1985; Teh and Houlsby, 1991).

As the characteristic length scale increases, as seen in the results of the bottom row of Fig. 9, the pattern of the deviatoric plastic strain is significantly different. At the same penetration depths, the plastic region still shows some faint hint of strain localization close to the piezocone sleeve, but the deformations below the cone evolve in a much more regular fashion. This is a consequence of the fact that the shear band width increases with ℓ_c, as shown by Oliynyk et al. (2022). With the value of ℓ_c/R adopted in simulation r302 the thickness of the eventual shear bands is a significant fraction of the cone radius, and therefore the bands are almost undetectable.

The effect of the initial bond strength on the accumulated plastic deviatoric deformations is shown in Fig. 10, where the results of simulation r102 on a strongly structured clay ($P_{t0} = 60$ kPa, top row in the figure) are compared with those of simulation r104, performed with the same characteristic length but assuming a much smaller initial bond strength ($P_{t0} = 5$ kPa, bottom row in the figure). While the magnitude of E_s^p appears comparable, the most notable difference between the two simulations is that, as the cone penetration progresses, no clear strain localization is visible in the results of simulation r104. This is most likely a consequence of the smaller amount of softening associated

[1] Selected animations of the results obtained in simulation r102 are provided as supplementary material, see Appendix C.

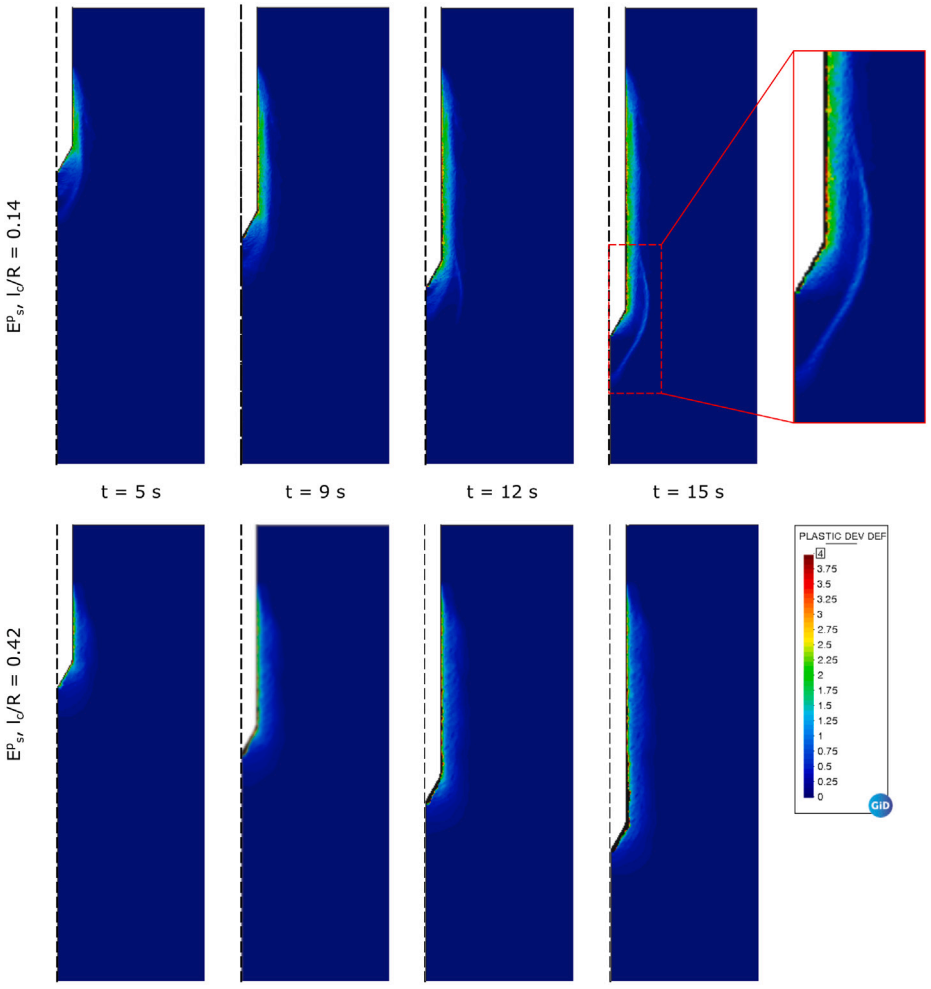

Fig. 9. Contour maps of accumulated plastic deviatoric strain E_s^p at different time stations, for simulation r102 (ℓ_c/R = 0.14) and r302 (ℓ_c/R = 0.42), with P_{t0} = 60 kPa.

to the debonding process experienced by the weakly structured soil as compared to the strongly structured one. This, in turns, yields a higher plastic modulus and reduces the likelihood of meeting the bifurcation condition which triggers the localization of deformations into shear bands (see, *e.g.*, Vardoulakis and Sulem, 1995).

Jacobian determinant of the deformation

In all the simulations of the CPTu tests, a relatively large value of the hydraulic conductivity k_h was adopted to account for the presence of a large silt fraction (see Table 2). A consequence of this assumption is that the local deformation process around the advancing cone tip may not occur in fully undrained (isochoric) conditions, and some local drainage may occur between contracting and dilating zones, as observed by Paniagua et al. (2013) in a small scale experiment on silty soil.

To investigate this aspect, the contour maps of the Jacobian determinant of the deformation, J, are plotted in Figs. 11 and 12 for some selected simulations. In both figures, the sign convention of continuum mechanics is adopted, in which a value of $J < 1$ indicates contraction while $J > 1$ denotes dilation. Fig. 11 shows the results of simulations r102 and r302, performed with the same initial bond strength (P_{t0} = 60 kPa) and the two extreme values of the normalized characteristic length (ℓ_c/R = 0.14 and 0.42, respectively). Fig. 12 shows the results of simulations r102 and r104, performed with the same value of the normalized characteristic length (ℓ_c/R = 0.14) and the two extreme values of the initial bond strength (P_{t0} = 60 and 5 kPa, respectively).

The results on the top row of Fig. 11, obtained with the smallest value of the normalized characteristic length, show that contractant and dilatant zones can be clearly identified in the soil around the cone tip. It is worth noting that the shape and size of these zones tend to follow the pattern of shear localization observed for E_s^p in the same simulation (see Fig. 9). In particular, the contractant zones below the cone base almost coincide with the observed shear bands, indicating that the localized shear deformation is accompanied by a permanent reduction in volume (contractant shear band). On the contrary, a small dilation is observed in both the regions between the shear bands and in a relatively large zone of soil outside the outermost shear band. Close to the piezocone shaft, as expected, a significant volume contraction is observed in a radially symmetric region with thickness of about one radius R, while the soil outside experience a small dilation up to a distance of about $6R$.

The effect of the characteristic length scale on volumetric deformations can be assessed by comparing the results of simulation r102 with those of simulation r302, shown in the bottom row of Fig. 11, obtained with the largest value of the normalized characteristic length. In this last case, the pattern of the Jacobian field J around the cone tip is quite different from the one observed for the smallest ℓ_c/R value. However, in this case it is possible to identify clearly the presence of alternate compaction and dilation zones, closer to the cone surface than in the previous case. While the contour maps of E_s^p did not show any substantial evidence of shear localization for r302, the volumetric deformations show that localization does indeed take place even for ℓ_c/R = 0.42, but in the form of compaction bands.

In Fig. 12, the effect of the initial bond strength on the Jacobian of the deformation is explored by comparing the results of simulation

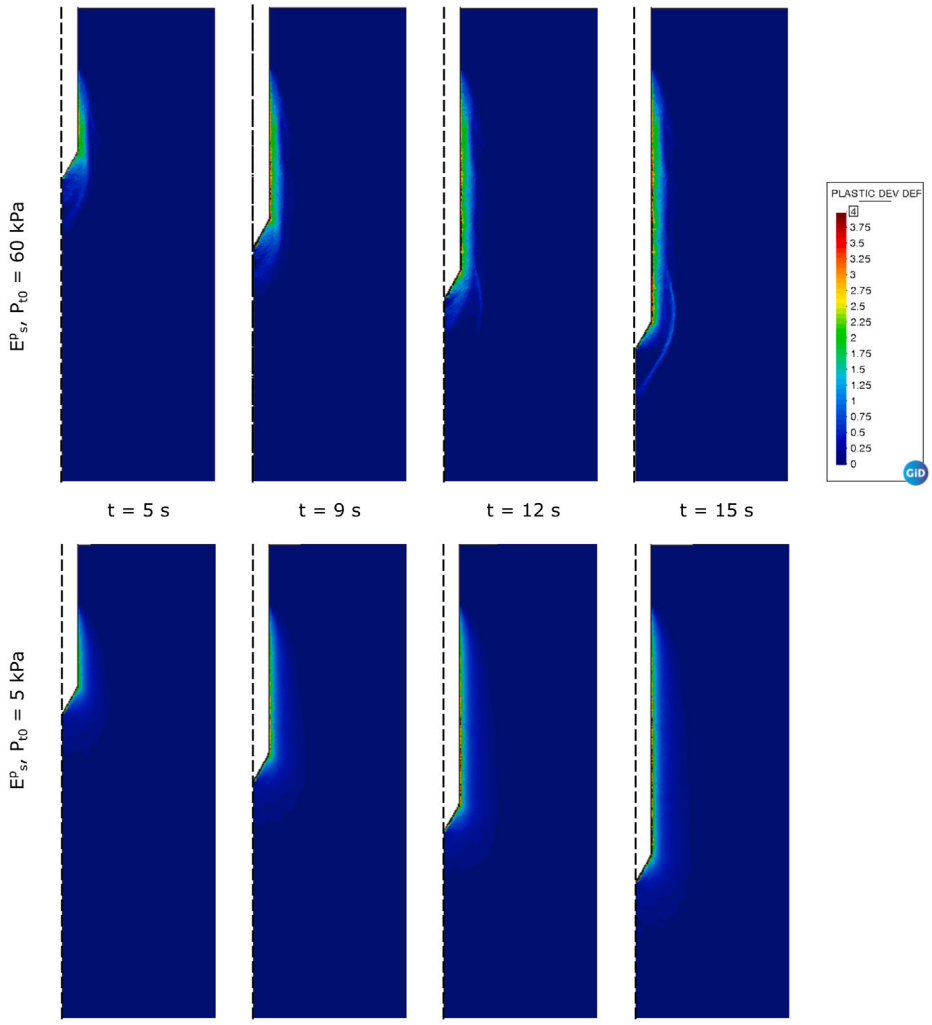

Fig. 10. Contour maps of accumulated plastic deviatoric strain E_s^p at different time stations, for simulation r102 (P_{t0} = 60 kPa) and r104 (P_{t0} = 5 kPa), with ℓ_c/R = 0.14.

r102 (P_{t0} = 60 kPa, top row) with those of simulation r104, adopting the same characteristic length but assuming a much smaller initial bond strength (P_{t0} = 5 kPa, bottom row). For the weakly structured soil, no significant evidence of the presence of localized volumetric deformations can be observed. The Jacobian field around the advancing cone tip is much more regular and the contour maps tend to follow the piezocone shape. Again, this could be attributed to the smaller amount of softening associated to the debonding process experienced by the weakly structured soil, which reduces the likelihood of triggering the formation of compaction bands.

Bond strength degradation

An important aspect of CPTu modeling in structured soils is that the large deformations induced by the cone penetration process are likely to be associated to significant destructuration effects in the region of soil close to the piezocone tip and shaft.

For the Osaka clay soil, this aspect is investigated in Figs. 13 and 14, which show the contour maps of bond strength, P_t for some selected simulations. The results of simulations r102 and r302, performed with the same initial bond strength (P_{t0} = 60 kPa) and the two extreme values of the normalized characteristic length (ℓ_c/R = 0.14 and 0.42, respectively) are displayed in Fig. 13. Fig. 14 provides the results of simulations r102 and r104, performed with the same value of the normalized characteristic length (ℓ_c/R = 0.14) and the two extreme values of the initial bond strength (P_{t0} = 60 and 5 kPa, respectively).

From the results of the simulation in the top row of Fig. 13, performed with the smallest characteristic length, it can be observed that the destructuration process going on around the advancing piezocone is indeed quite strong. Almost complete degradation of the bond strength is occurring in a zone of soil which extends below the cone tip by 2–3 times the cone radius R, and laterally by about one cone radius from the piezocone shaft. As expected, the geometry of the destructured soil regions closely follow the pattern of shear bands observed in Fig. 9, where the amount of accumulated plastic deformation is maximum. The comparison of the snapshots corresponding to the different penetration depths allow to visualize clearly the progressive formation and propagation of the localization zones with time.

In the case at hand, the destructuration process is mainly associated to distortional plastic deformations which are much larger in absolute value than the volumetric deformations. Therefore, when the characteristic length scale increases, as in simulation r302 (bottom row of Fig. 13), the pattern of bond strength is much more regular, reflecting the absence of localized shear deformations observed in Fig. 9. This result is similar to the one obtained by Hauser and Schweiger (2021) in their PFEM simulations of CPTu tests in clay, performed with a non-local version of the CASM model, adopting normalized characteristic length values in the range between 0.27 and 0.40.

The lack of clearly apparent localized deformation zones in the simulation r104, performed with a low initial bond strength, gives rise to a similar pattern of soil destructuration around the piezocone tip and shaft, as shown in the bottom row of Fig. 14. In this case the size

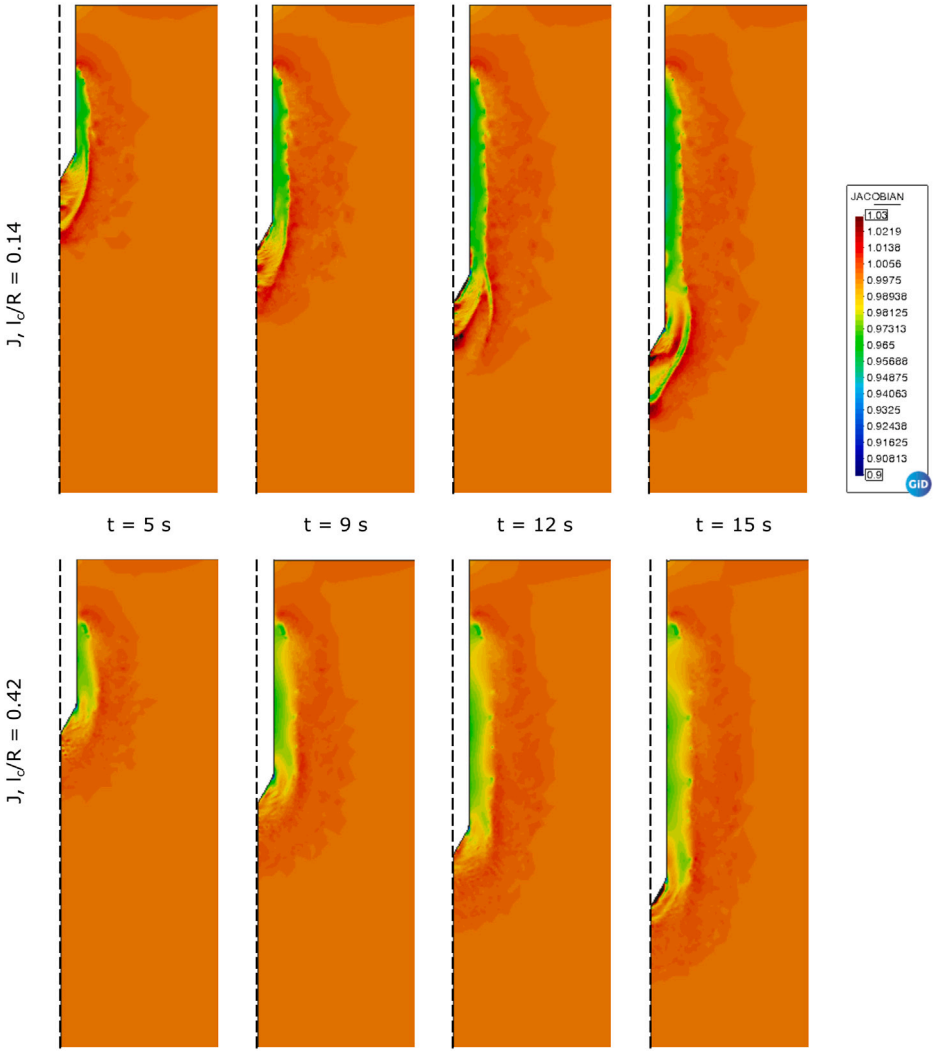

Fig. 11. Contour maps of Jacobian determinant J at different time stations, for simulation r102 (ℓ_c/R = 0.14) and r302 (ℓ_c/R = 0.42), with P_{t0} = 60 kPa. In the figure, J is represented using the solid mechanics convention ($J > 1$ for dilation).

of the fully destructured region extends laterally a little bit further, as compared to that of simulation r102 (top row of the same figure).

Excess pore water pressures

Despite of the relatively high permeability adopted for the soil, the penetration process induces significant excess pore pressures in the soil region close to the advancing cone tip. In actual CPTu tests, this quantity can be monitored at two different positions along the cone surface (probes 1 and 2 in Fig. 8).

Figs. 15 and 16 show the contour maps of the excess pore water pressure, Δu, for some selected simulations.[2] As for the other field variables considered, the results of simulations r102 and r302, performed with the same initial bond strength (P_{t0} = 60 kPa) and the two extreme values of the normalized characteristic length (ℓ_c/R = 0.14 and 0.42, respectively) are displayed in Fig. 15. Fig. 16 provides the results of simulations r102 and r104, performed with the same value of the normalized characteristic length (ℓ_c/R = 0.14) and the two extreme values of the initial bond strength (P_{t0} = 60 and 5 kPa, respectively).

Fig. 15 shows the effects of the adopted characteristic length on the computed excess pore pressures. For both simulations r102 (top row) and r302 (bottom row), the minimum (compressive) excess pore pressure is obtained at the cone surface-soil interface, approximately at the position of probe 1. The shape and size of the contours are also quite similar and change relatively little with advancement depth and with ℓ_c/R. Differently from the deformation and bond strength fields, no evidence of concentration of Δu into thin zones is apparent, even in the case of simulation r102, due to local pore pressure diffusion effects. The most significant differences in the two cases reported in the figure are: the magnitude of positive excess pore pressures (associated to dilation) detected in a small region around the cone axis ahead of the cone tip, much higher in the case of the smaller characteristic length; and in the size of the zone characterized by large compressive values of Δu at the cone flank, which is wider in the case of the larger characteristic length.

The effect of the initial bond strength on the excess pore water pressure is shown in Fig. 16, where the results of simulation r102, with P_{t0} = 60 kPa (top row) are compared with those of simulation r104, performed with the same characteristic length but assuming a much smaller initial bond strength (P_{t0} = 5 kPa, bottom row).

While the shape and position of the contours of excess pore pressure are similar for both values of P_{t0} considered, the striking difference is in the respective range of values for Δu. In particular, the minimum (compressive) Δu at the cone mid-height is about 100 kPa smaller (that is, 100 kPa larger in absolute value) for the heavily structured soil as compared to the weakly structured soil. This is due to the fact that the

[2] Note that, in both figures, the continuum mechanics sign convention (compression negative) is adopted in the representation of Δu.

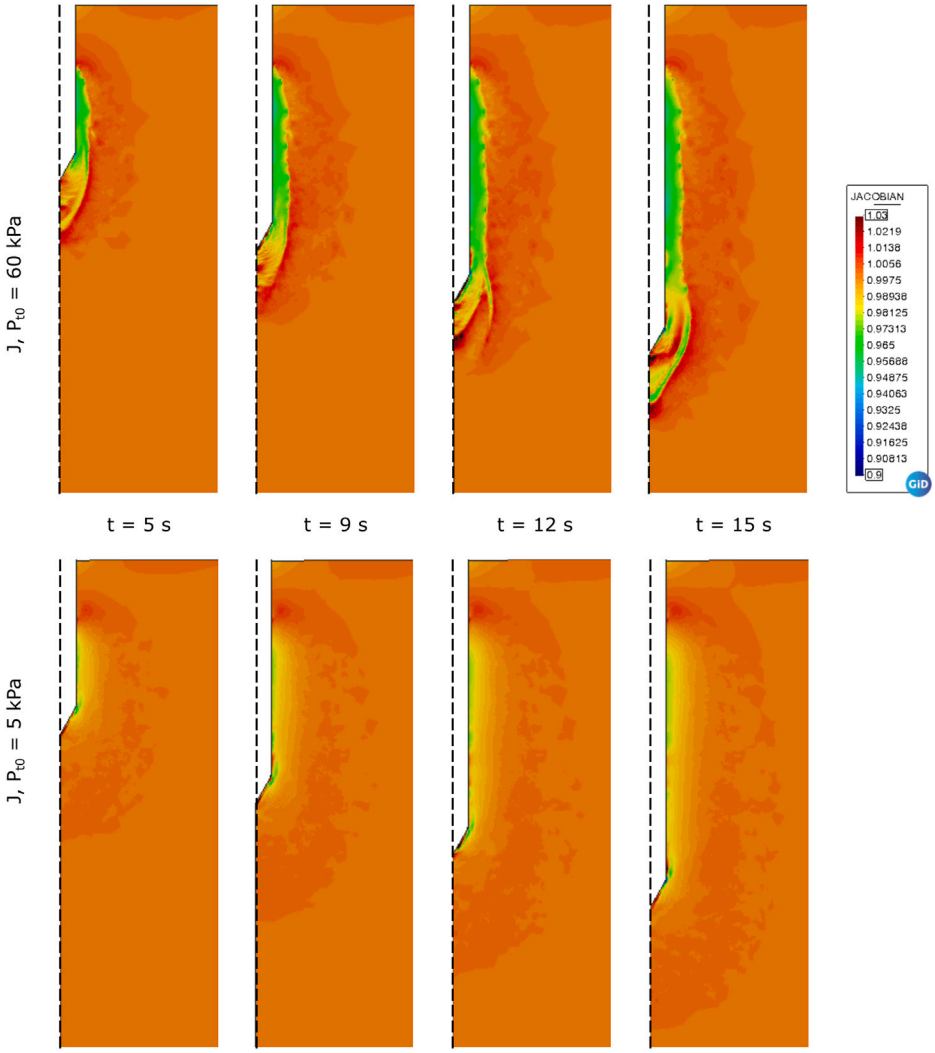

Fig. 12. Contour maps of Jacobian determinant J at different time stations, for simulation r102 (P_{t0} = 60 kPa) and r104 (P_{t0} = 5 kPa), with ℓ_c/R = 0.14. In the figure, J is represented using the solid mechanics convention ($J > 1$ for dilation).

total stresses around the cone tip increase in magnitude with increasing bond strength, and so does the excess pore pressure in almost undrained conditions.

6.2. Conventional interpretation of CPTu simulations

In this section, a selection of results from the different simulations performed is shown in terms of the typically measured quantities in real CPTu tests:

(a) the net cone resistance, defined as:

$$q_n = q_c - \sigma^*_{z0} \tag{2}$$

where q_c is the cone resistance and σ^*_{z0} is the total initial vertical stress at the measurement depth;

(b) the excess pore water pressure registered at the location of probe 1, Δu_1,

as functions of the normalized cone penetration depth $Z = (z - z_0)/R$. In order to filter out small numerical oscillations due to remeshing at the soil-cone interface, the values of q_n and Δu_1 have been smoothed using a mobile average with Z, as suggested in Monforte et al. (2018a).

In all the simulations, both q_n and Δu_1 profiles are characterized by an initial transient stage, up to $Z = -4$, followed by a stationary state up to the final value of the penetration depth. Their average values, $\overline{q}_n$ and $\overline{\Delta u}_1$, over the range $-4 \geq Z \geq -19$ are reported in Table 5.

Table 5
CPTu tests simulations on Osaka clay: average values of net cone resistance and excess pore pressure evaluated at probe 1 over the interval $Z \in [-19, -4]$.

Test #	ℓ_c/R (–)	P_{t0} (kPa)	$\overline{q}_n$ (kPa)	$\overline{\Delta u}_1$ (kPa)
r102	0.14	60.0	558.49	436.02
r202	0.28	60.0	572.50	440.66
r302	0.42	60.0	570.53	461.08
r103	0.14	30.0	514.21	375.81
r203	0.28	30.0	525.30	392.84
r303	0.42	30.0	535.96	390.54
r104	0.14	5.0	456.03	338.83
r204	0.28	5.0	472.94	327.91
r304	0.42	5.0	466.32	332.72

The effect of the characteristic length on the computed values of q_n and Δu_1 can be assessed by looking at the results shown in Fig. 17, which refers to simulations r103, r203 and r303, performed with different values of ℓ_c/R and P_{t0} = 30 kPa (see Table 4). Similar results are obtained for the other two values of the initial bond strength considered.

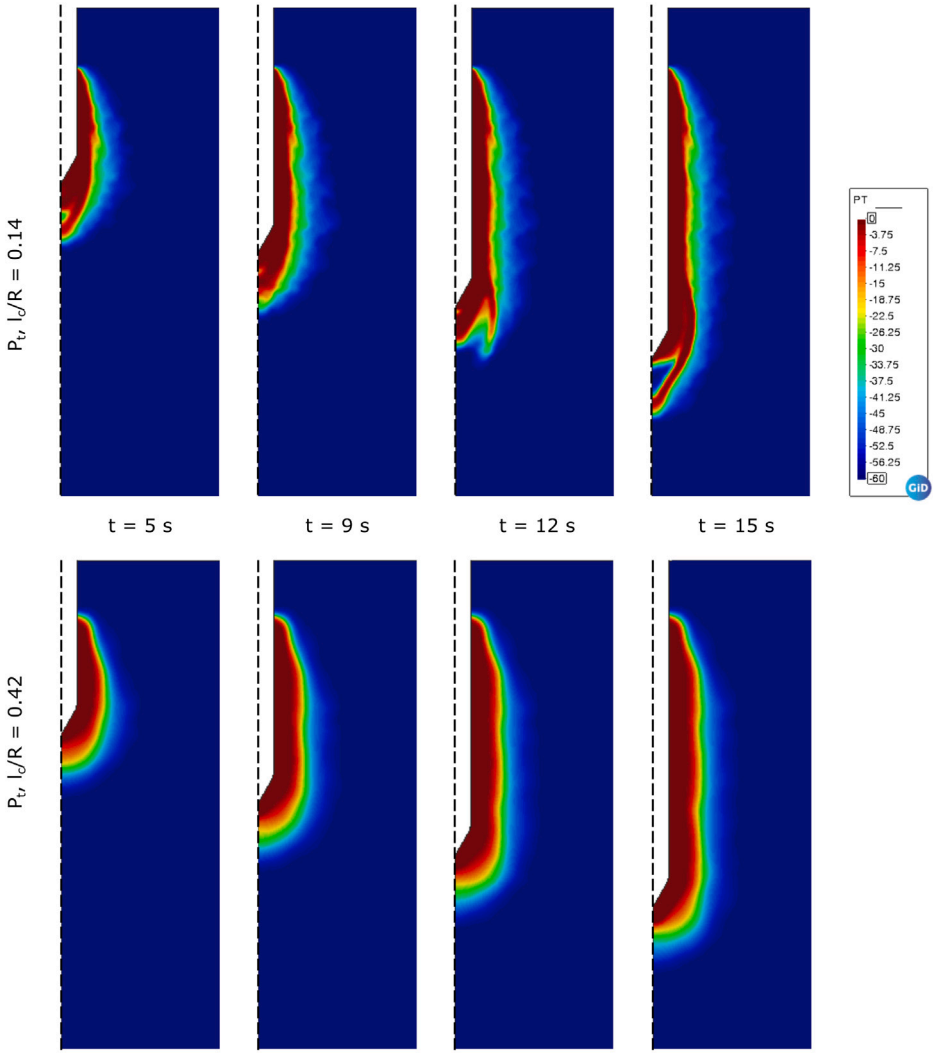

Fig. 13. Contour maps of bond strength P_t at different time stations, for simulation r102 ($\ell_c/R = 0.14$) and r302 ($\ell_c/R = 0.42$), with $P_{t0} = 60$ kPa. In the figure, P_t is represented using the solid mechanics convention (tension positive).

From the figure, it can be observed that the adopted value of the characteristic length has only a minor impact on the test results, in terms of both $\overline{q}_n$ and $\overline{\Delta u}_1$. The only significant (yet small difference) is observed in the net cone resistance as ℓ_c/R is varied. The data reported in Table 5 indicate that the simulations performed with $\ell_c/R = 0.28$ and 0.42 provide 2 to 4% larger average values of $\overline{q}_n$ for the same initial bond stress level. As for the computed average values of Δu_1, no similar trend is observed. In fact, the value of $\overline{\Delta u}_1$ obtained with $\ell_c/R = 0.14$ in simulation r104, with $P_{t0} = 5$ kPa, is the largest among those obtained with larger characteristic length at the same initial bond strength; however, the opposite is true for the two other groups of simulations performed with larger initial bond strength, see Table 5.

As expected, the assumed initial bond strength has a much larger impact on the simulation results. This is clearly shown in Fig. 18, which reports the computed profiles of q_n and Δu_1 for different values of P_{t0} and $\ell_c/R = 0.14$ (simulations r102, r103 and r104). Similar results are obtained for the other two values of the characteristic length considered.

Both the net cone resistance and the excess pore pressure at probe 1 increase with the initial bond strength of the soil. However, it is worth noting that the differences between the values of q_n and Δu_1 registered in the three simulations considered are not very large, in spite of the significantly different P_{t0} values considered.

Some further insight on this point can be obtained by interpreting the test results in terms of existing correlations, widely used in practice, between the net cone resistance and some conventional indicators of the soil "strength" such as:

(a) the undrained shear strength of the soil as measured in triaxial undrained compression tests, starting from the initial in-situ state, determined as $s_u = q_f/2$, where q_f is the deviator stress at failure;
(b) the effective yield stress σ_y as measured in one-dimensional (oedometric) compression tests, starting from the initial in-situ state.

Both s_u and σ_y are not material properties, but define some specific behavior of the soil which is affected by the size of the yield surface, and thus by the degree of structure possessed by the soil.

In order to obtain the reference values of s_u and σ_y for the Osaka clay, a series of unconsolidated undrained TX tests and oedometric tests were simulated with the FD_Milan model, starting from the initial states considered in the CPTu tests program. As the soil response in undrained TX tests was characterized by stress–strain curves showing a peak and a subsequent strength reduction up to the critical state, both peak (s_u^p) and ultimate (s_u^u) values of undrained strength were defined for each test. The reference values of s_u^p, s_u^u and σ_y thus obtained are summarized in Table 6.

In geotechnical engineering practice, the following conventional expression are adopted to determine the undrained shear strength of

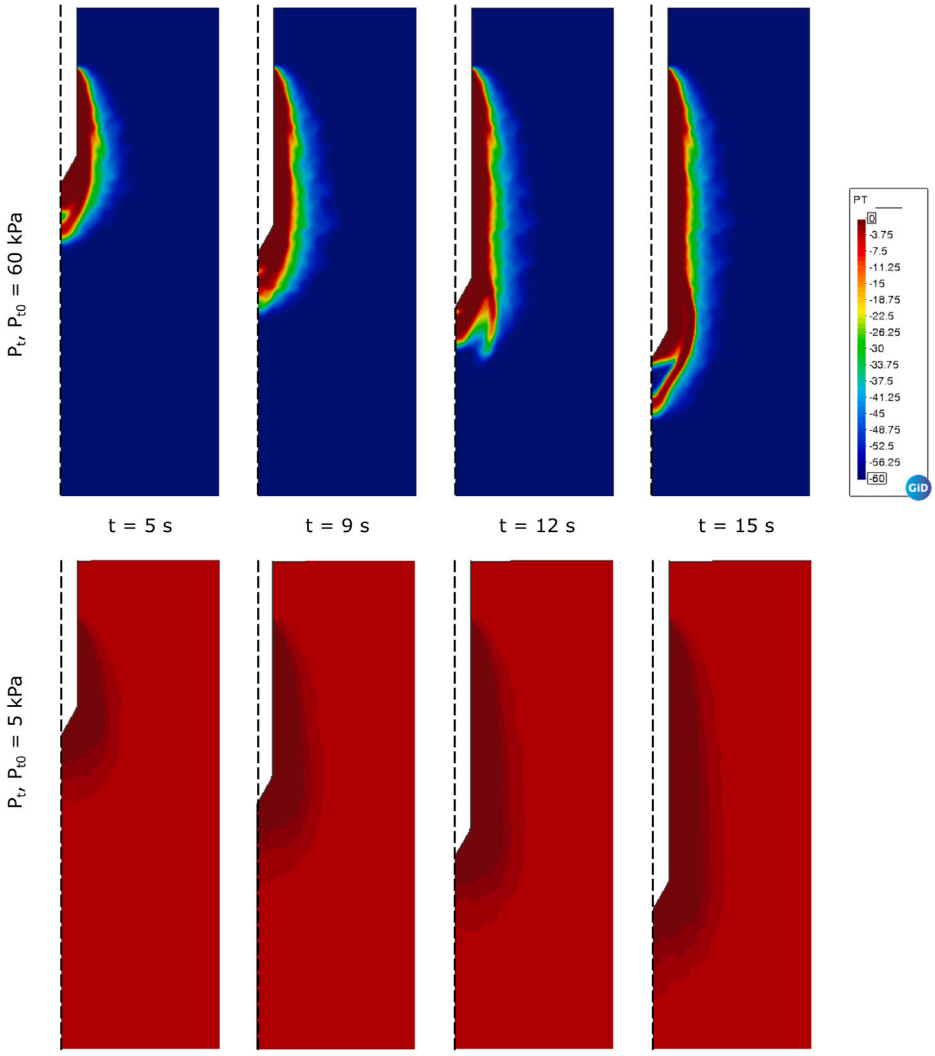

Fig. 14. Contour maps of bond strength P_t at different time stations, for simulation r102 (P_{t0} = 60 kPa) and r104 (P_{t0} = 5 kPa), with ℓ_c/R = 0.14. In the figure, P_t is represented using the solid mechanics convention (tension positive).

Table 6
Reference values of s_u^p, s_u^u and σ_y as obtained from simulations of undrained TX and oedometric tests on Osaka clay, for the 3 different initial conditions assumed in the CPTu test simulations.

σ_z (kPa)	σ_r (kPa)	P_{t0} (kPa)	P_{s0} (kPa)	s_u^p (kPa)	s_u^u (kPa)	σ_y (kPa)
100.0	60.0	60.0	120.0	120.84	42.42	525.49
100.0	60.0	30.0	120.0	85.15	42.42	317.69
100.0	60.0	5.0	120.0	50.66	42.42	169.92

the soil from the CPTu test results:

$$s_u = \frac{q_n}{N_c} \qquad s_u = \frac{\Delta u_i}{N_{\Delta u}} \quad (i = 1, 2) \tag{3}$$

where N_c and $N_{\Delta u}$ are dimensionless quantities known as cone factors. Starting from these expressions, the undrained strength data in Table 6 can be used to define the following normalized net cone resistance and excess pore pressure values at probe 1, for both peak and critical state (ultimate) conditions:

$$N_c^p = \frac{q_n}{s_u^p} \qquad N_c^u = \frac{q_n}{s_u^u} \tag{4}$$

$$N_{\Delta u}^p = \frac{\Delta u_1}{s_u^p} \qquad N_{\Delta u}^u = \frac{\Delta u_1}{s_u^u} \tag{5}$$

These four dimensionless quantities, computed for the three simulations with ℓ_c/R = 0.14, are shown in Figs. 19 and 20.

From the results in Fig. 19 it can be noted that, when the values of q_n are normalized with respect to the peak undrained strength, the values of N_c^p decrease significantly with increasing initial bond strength, passing from about 9 for P_{t0} = 5 kPa to about 5 for P_{t0} = 60 kPa. This is due to the fact that s_u^p is conventionally determined when the soil is at the first yield state or close to it, and the destructuration of the soil is either zero or very small. However, as clearly shown by the results in Fig. 14, when the soil is heavily structured a significant amount of destructuration takes place in the soil ahead of the cone tip, while this effect is much smaller in weakly structured soils.

The opposite is observed when the values of q_n are normalized with respect to the ultimate undrained strength, since the values of N_c^u increase with increasing initial bond strength, passing from about 10 for P_{t0} = 5 kPa to about 13 for P_{t0} = 60 kPa. This is not surprising, since even the very large deformation levels induced in the soil by the cone advancement are not sufficient to cause the complete destructuration of the soil region determining the stress state acting on the cone. Thus, the larger the initial bond strength, the larger is the residual amount of structure which affects the net cone resistance.

It is worth noting that, in his overview of the literature on the interpretation of CPT tests in clays, Salgado (2022) reports that the N_c coefficient typically falls in the range between 9 and 15. The values of

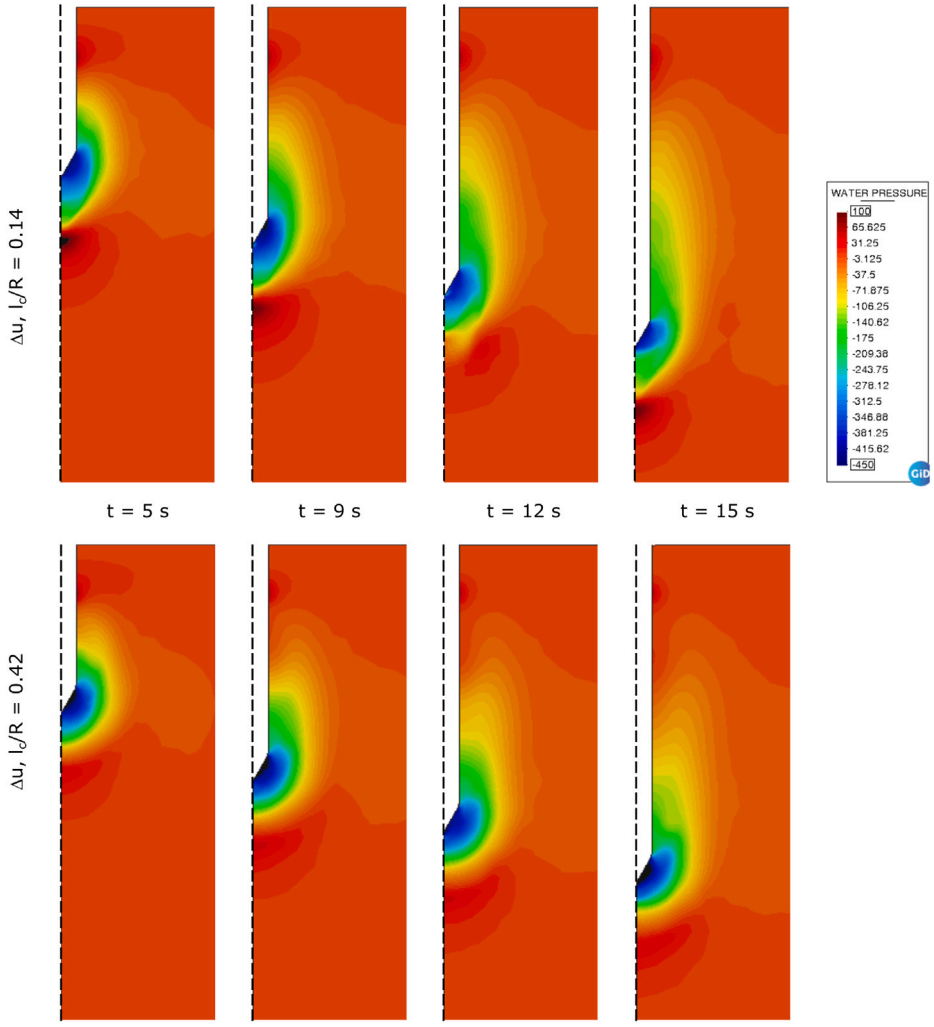

Fig. 15. Contour maps of excess pore water pressure Δu at different time stations, for simulation r102 (ℓ_c/R = 0.14) and r302 (ℓ_c/R = 0.42), with P_{t0} = 60 kPa. In the figure, Δu is represented using the solid mechanics convention (tension positive).

N_c^u reported in Fig. 19 fall within this range, while the N_c^p values for the cases with P_{t0} equal to 30 and 60 kPa are significantly lower. This means that a conventional interpretation of q_n measurements in heavily structured clay with a value N_c in the range suggested by Salgado would provide a significant underestimation of the peak undrained strength. The s_u values obtained would rather be closer to the ultimate undrained shear strength of the soil.

The data in Fig. 20, referring to the profiles of the normalized excess pore pressure $N_{\Delta u}^p$ and $N_{\Delta u}^u$, show a similar trend of variation with P_{t0} as the normalized net cone resistance values. When the values of Δu_1 are normalized with respect to the peak undrained strength, the values of $N_{\Delta u}^p$ decrease significantly with increasing initial bond strength, while the opposite is observed when the values of Δu_1 are normalized with respect to the ultimate undrained strength. This is due to the fact that the excess pore water pressures measured at the probes increase with the net cone resistance, and thus are affected by the soil destructuration around the cone tip in the same way as q_n.

A correlation between the net cone resistance and the yield stress σ_y as measured in oedometric tests has been proposed by Mayne for non-structured, inorganic clays (Mayne, 1991, 2005), and more recently reviewed by Mayne and Agaiby (2019) to extend it to organic clays. The different correlations proposed are represented graphically in Fig. 21.

In the same figures are also plotted the points of coordinates $(\bar{q}_n, \sigma_y)$ corresponding to each CPTu simulations, with the average cone resistance values of Table 5. The data points plotted with circles, corresponding to the simulations performed on the weakly structured soil, fit very nicely with Mayne's correlation for unstructured clays. However, all the other data points (triangles for P_{t0} = 30 kPa and squares for P_{t0} = 60 kPa) are located to the left of the correlation. This indicates that the measured average net cone resistance is smaller than what Mayne's correlation would predict for the given yield stresses σ_y, the difference increasing as P_{t0} increases. As the yield stress in oedometric compression is determined at the first yield point, when the soil has not yet undergo any destructuration, this result is in line with the previous observations made on the normalized peak cone resistance N_c^p. In fact, the computed values of $\bar{q}_n$ are significantly affected by the destructuration process going on in the soil around the advancing cone, which is more intense for heavily structured soils than for weakly structured soils. An important practical consequence of this observation is that the use of Mayne's correlation on heavily structured soils may provide largely underestimated values of σ_y, and thus of the overconsolidation ratio OCR of the soil deposit.

7. Concluding remarks

The response of a natural structured clay to the penetration of the piezocone in CPTu tests was investigated by means of a series of fully coupled, non-linear hydrodynamic PFEM simulations, incorporating an isotropic hardening elastoplastic constitutive model based on the multiplicative decomposition of the deformation gradient. In the model,

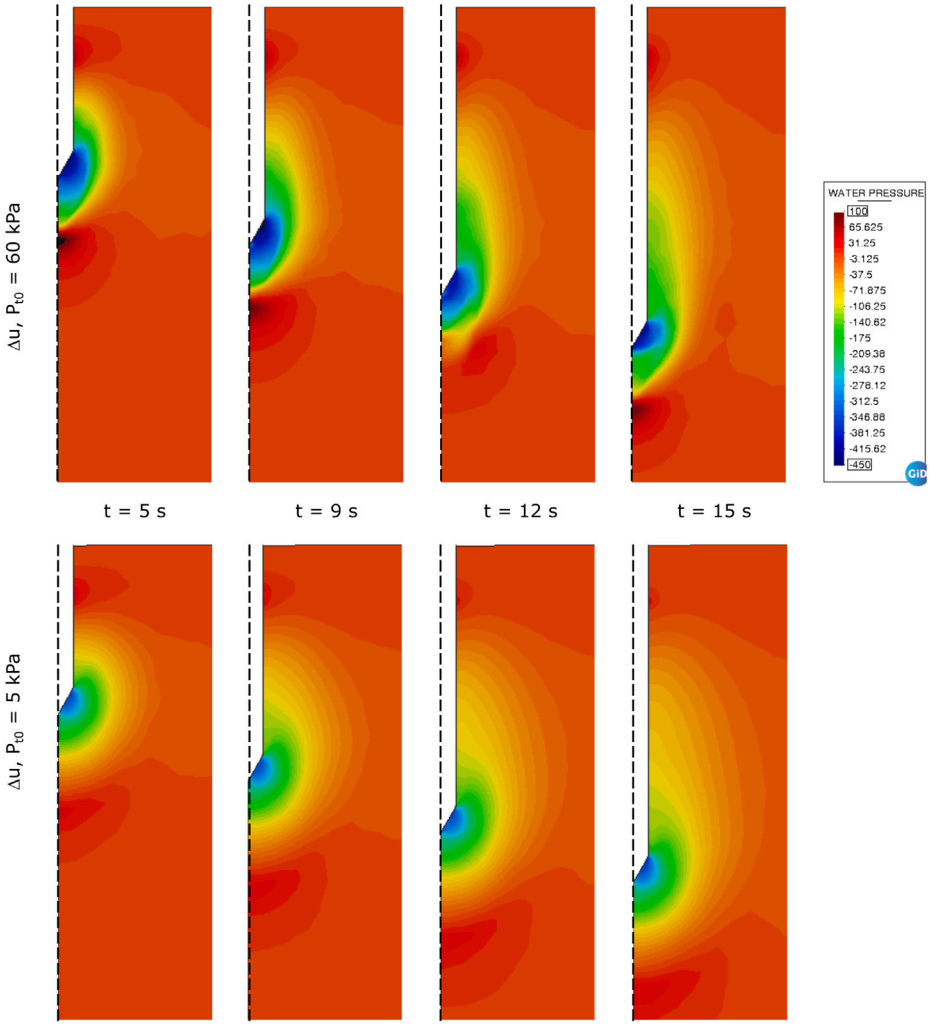

Fig. 16. Contour maps of excess pore water pressure Δu at different time stations, for simulation r102 (P_{t0} = 60 kPa) and r104 (P_{t0} = 5 kPa), with ℓ_c/R = 0.14. In the figure, Δu is represented using the solid mechanics convention (tension positive).

the effects of structure are quantified by means of a specific internal variable – the bond strength – which decreases monotonically with increasing accumulated plastic strains.

As the destructuration process can be accompanied by significant strain softening – which may trigger the spontaneous localization of the deformations into shear bands – the model was equipped with a non-local formulation of the hardening laws, which provides the material with the necessary internal length scale regularizing the numerical solution in the post-localization regime.

The results obtained in this study show that the kinematics of the deformation process around the advancing cone tip can be strongly affected by the ratio between the characteristic length ℓ_c and the cone radius R. In particular, for heavily structured soils (high initial bond strength P_{t0}), when ℓ_c is relatively small with respect to R, the accumulated plastic deviatoric deformation field is characterized by clearly visible shear bands, which originate in correspondence of the piezocone sleeve and then propagate downwards until they reach the cone axis well below the cone tip. For larger values of ℓ_c, at the same initial P_{t0}, no localized deviatoric deformation zones can be detected, and the E_s^p field is much more regular around the cone tip. This is due to the fact that as ℓ_c increases, so does the shear band width, which may eventually become of size comparable to the cone radius.

Significant strain localization is also observed, for the same initial bond strength, in the volumetric deformations. The localized volumetric deformation zones below the cone base almost coincide with the previously observed shear bands, indicating that the localized shear deformation is accompanied by a permanent reduction in volume (contractant shear bands). Volumetric deformation bands (compaction bands) are also observed in the case of the largest ℓ_c value considered, although of smaller length and closer to the cone surface than in the previous case. No significant strain localization in both deviatoric and volumetric components is observed in the case of weakly structured soil (low initial bond strength P_{t0}).

It is worth noting that, in presence of shear bands, the deformation field is not stationary around the advancing cone tip, as it is assumed in some CPTu modeling approaches based on the theory of cavity expansion or on the Strain Path Method.

When deviatoric deformations are localized into shear bands, the spatial distribution of the bond strength closely follows the localization zones, with the smaller values (higher destructuration) found in correspondence of the interior of the bands. In general, regardless of the initial amount of structure or the soil characteristic length, the soil around the advancing piezocone is subjected to a very strong destructuration process, leading to the complete loss of bond strength.

Quite surprisingly, the large differences in the kinematics of the deformation process around the cone tip observed in the simulations as the characteristic length is reduced are not reflected in the calculated net cone resistance q_n and in the excess pore pressure Δu_1 measured at the cone mid-height, which are practically independent of ℓ_c.

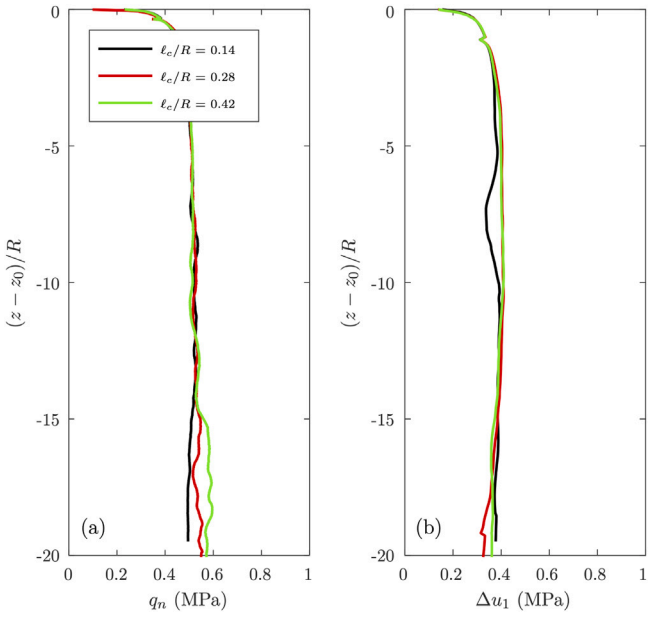

Fig. 17. Results of simulations r103, r203 and r303 with P_{t0} = 30 kPa and different normalized characteristic lengths ℓ_c/R. Profiles with depth of: (a) net cone resistance q_n; (b) excess pore pressure at the cone mid-height Δu_1.

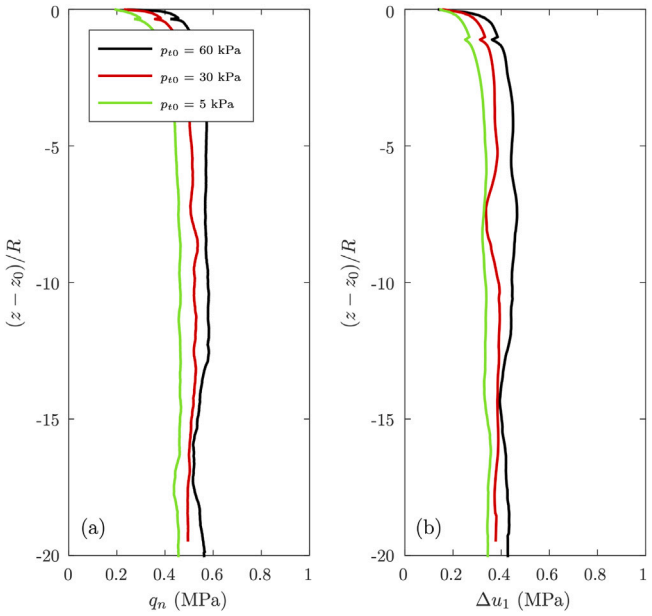

Fig. 18. Results of simulations r102, r103 and r104 with ℓ_c/R = 0.14 and different initial bond strength P_{t0}. Profiles with depth of: (a) net cone resistance q_n; (b) excess pore pressure at the cone mid-height Δu_1.

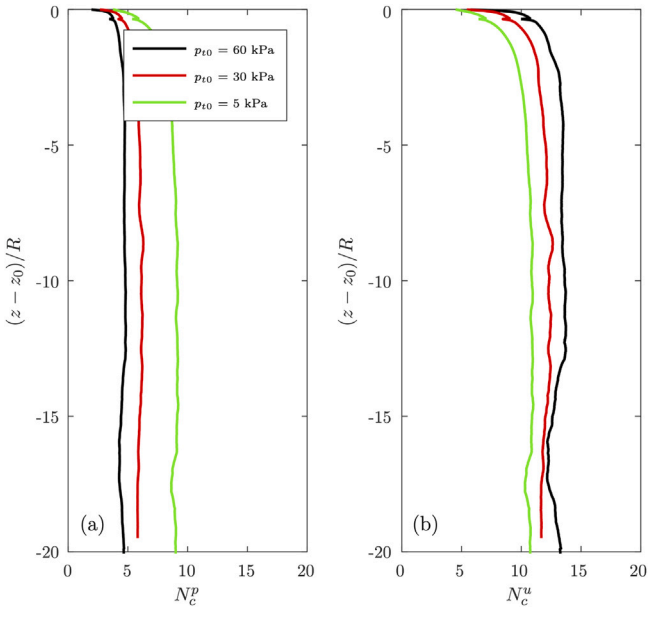

Fig. 19. Results of simulations r102, r103 and r104, with ℓ_c/R = 0.14. Profiles with depth of net cone resistance, q_n, normalized with respect to: (a) the peak undrained strength s_u^p; (b) the ultimate undrained strength s_u^u.

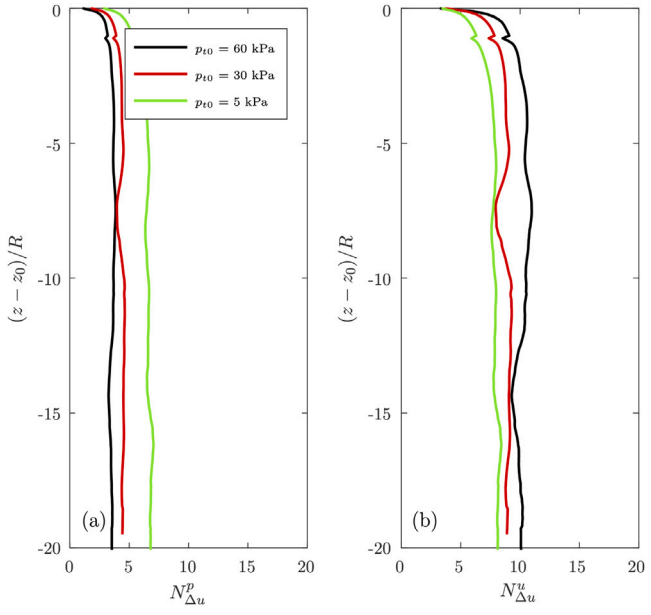

Fig. 20. Results of simulations r102, r103 and r104, with ℓ_c/R = 0.14. Profiles with depth of excess pore water pressure at probe 1, Δu_1, normalized with respect to: (a) the peak undrained strength s_u^p; (b) the ultimate undrained strength s_u^u.

On the contrary, the initial degree of structure possessed by the soil has a clear effect on q_n and Δu_1, which increase with increasing initial bond strength P_{t0}. However, the interpretation of the computed net cone resistance values in terms of existing correlations with conventional soil properties – the undrained strength s_u and yield stress in one-dimensional compression σ_y – indicates that this effect is not as large as one might have expected. This is a consequence of the significant amount of destructuration that the soil experiences during the piezocone advancement.

For the particular natural soil examined, the results obtained show that the use of N_c values reported in the literature in the interpretation of the CPTu test results would provide an undrained strength s_u value closer to the ultimate undrained shear strength of the soil. At the same time, the use of Mayne and Agaiby (2019) correlation to estimate σ_y would lead to a significant underestimation of the overconsolidation ratio OCR of the soil.

These results represent a promising step towards a more rational interpretation of the CPTu tests in structured geomaterials and for their use in the calibration of advanced soil models.

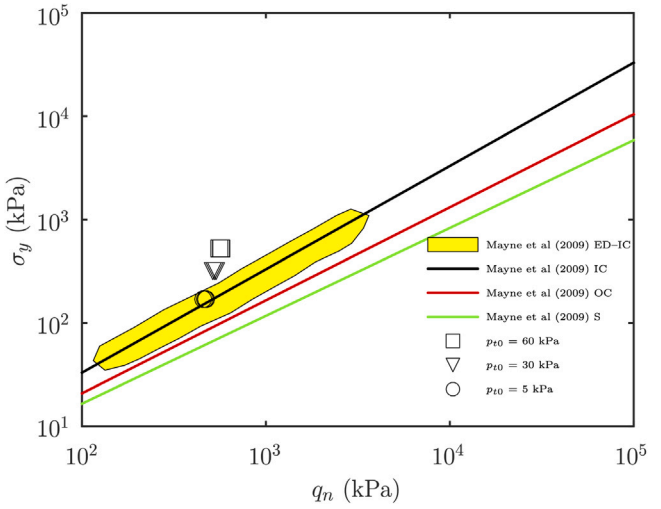

Fig. 21. Effective yield stress σ_y – as determined in oedometric compression tests for the assumed initial states – *vs.* average net cone resistance, $\bar{q}_n$. The shaded area (ED-IC) represents the range of experimental data reported by Mayne et al. (2009) for intact, unstructured inorganic clays. The full curves refer to the correlations proposed by Mayne et al. (2009): IC = intact non-structured inorganic clays; OC = organic clays; S = silts.

CRediT authorship contribution statement

Kateryna Oliynyk: Writing – review & editing, Writing – original draft, Visualization, Validation, Software, Methodology, Investigation, Formal analysis, Conceptualization. **Matteo O. Ciantia:** Writing – review & editing, Writing – original draft, Visualization, Validation, Resources, Methodology, Investigation, Funding acquisition, Formal analysis, Conceptualization, Supervision. **Claudio Tamagnini:** Conceptualization, Data curation, Formal analysis, Funding acquisition, Methodology, Resources, Writing – original draft, Writing – review & editing.

Declaration of competing interest

The authors declare that they have no known competing financial interests or personal relationships that could have appeared to influence the work reported in this paper.

Data availability

Data will be made available on request.

Acknowledgments

The first author gratefully acknowledges the financial support of the grant "Constitutive modeling of mechanical and chemical degradation processes in cemented soils and weak rocks in the framework of the theory of hyperplasticity in finite deformations" of the Civil and Environmental Engineering Department of the University of Perugia. The ICE-PICK project, funded by the EPSRC NIA grant EP/W00013X/1, along with the RSE Saltire International Collaboration Award, funded by the Royal Society Edinburgh, is also acknowledged.

Appendix A. Constitutive equations of the FD_Milan model

The FD_Milan model is based on the general framework of isotropic multiplicative finite deformation plasticity (Simo and Hughes, 1998; Borja, 2013) in which the deformation gradient $\boldsymbol{F}$ is multiplicatively decomposed into an elastic, reversible part $\boldsymbol{F}^e$ and a plastic, irreversible part $\boldsymbol{F}^p$:

$$\boldsymbol{F} = \boldsymbol{F}^e \boldsymbol{F}^p$$

The (hyper)elastic behavior of the model is defined in terms of an assumed free energy function of one of the elastic Cauchy–Green deformation tensors, $\boldsymbol{b}^e = \boldsymbol{F}^e \boldsymbol{F}^{eT}$ or $\overline{\boldsymbol{C}}^e = \boldsymbol{F}^{eT} \boldsymbol{F}^e$.

The evolution equations for the state variables, *i.e.*, the Kirchhoff stress tensor $\boldsymbol{\tau}$ and the scalar internal variables P_s (preconsolidation stress) and P_t (bond strength) are provided by:

$$\overset{\nabla}{\boldsymbol{\tau}} = \mathfrak{a}^{ep} \boldsymbol{d} \tag{6}$$

$$\dot{\boldsymbol{q}} = \dot{\gamma}\, \boldsymbol{h}(\boldsymbol{\tau}, \boldsymbol{q}) \tag{7}$$

In Eq. (6), $\overset{\nabla}{\boldsymbol{\tau}}$ is the Jaumann rate of the Kirchhoff stress tensor, given by:

$$\overset{\nabla}{\boldsymbol{\tau}} = \dot{\boldsymbol{\tau}} - \boldsymbol{w}\boldsymbol{\tau} + \boldsymbol{\tau}\boldsymbol{w}$$

$\boldsymbol{d} = \mathrm{sym}(\nabla \boldsymbol{v})$ is the symmetric part of the spatial velocity gradient, *i.e.*, the rate of deformation tensor, and $\boldsymbol{w} = \mathrm{skw}(\nabla \boldsymbol{v})$ is the spin tensor. The fourth-order spatial elastoplastic continuum tangent stiffness tensor, $\mathfrak{a}^{ep}$, is defined as:

$$\mathfrak{a}^{ep} = \begin{cases} \mathfrak{a}^e - \dfrac{1}{\hat{K}_p} \left(\mathfrak{a}^e \dfrac{\partial g}{\partial \boldsymbol{\tau}} \right) \otimes \left(\mathfrak{a}^e \dfrac{\partial f}{\partial \boldsymbol{\tau}} \right) & \text{if } (\partial f / \partial \boldsymbol{\tau}) \cdot \mathfrak{a}^e \boldsymbol{d} > 0 \\ \mathfrak{a}^e & \text{otherwise} \end{cases} \tag{8}$$

where $f(\boldsymbol{\tau}, \boldsymbol{q})$ is the yield function; $g(\boldsymbol{\tau}, \boldsymbol{q})$ is the plastic potential function, and $\hat{K}_p$ is a strictly positive scalar given by:

$$\hat{K}_p := \frac{\partial f}{\partial \boldsymbol{\tau}} \cdot \mathfrak{a}^e \frac{\partial g}{\partial \boldsymbol{\tau}} - \frac{\partial f}{\partial \boldsymbol{q}} \cdot \boldsymbol{h} > 0 \tag{9}$$

The spatial fourth-order elastic tangent stiffness tensor, $\mathfrak{a}^e$, appearing in Eqs. (8) and (9) is obtained from the free energy function $\bar{\Psi}^e_s(\overline{\boldsymbol{C}}^e)$ of the material (in the intermediate configuration) as:

$$\mathfrak{a}^e_{ijkl} = \mathbb{c}^e_{ijkl} + \tau_{ik}\delta_{jl} + \tau_{il}\delta_{jk} \tag{10}$$

$$\mathbb{c}^e_{ijkl} = 4 \frac{\partial^2 \bar{\Psi}^e_s}{\partial \overline{C}^e_{AB} \partial \overline{C}^e_{CD}} F^e_{iA} F^e_{jB} F^e_{kC} F^e_{lD} \tag{11}$$

in which $\overline{\boldsymbol{C}}^e = \boldsymbol{F}^{eT} \boldsymbol{F}^e$ is the right elastic Cauchy–Green deformation tensor.

In Eq. (7), the vectors $\boldsymbol{q}$ and $\boldsymbol{h}$ are defined as:

$$\boldsymbol{q} = \begin{Bmatrix} P_s \\ P_t \end{Bmatrix} \qquad \boldsymbol{h} = \begin{Bmatrix} h_s(\boldsymbol{\tau}, \boldsymbol{q}) \\ h_t(\boldsymbol{\tau}, \boldsymbol{q}) \end{Bmatrix} \tag{12}$$

and $\dot{\gamma} \geq 0$ is the plastic multiplier, given by:

$$\dot{\gamma} = \frac{1}{\hat{K}_p} \frac{\partial f}{\partial \boldsymbol{\tau}} \cdot \mathfrak{a}^e \boldsymbol{d} \geq 0 \tag{13}$$

The scalar functions h_s and h_t are the hardening functions of the preconsolidation stress P_s and of the bond strength P_t, introduced in Section 2.

A.1. Free energy function

Due to the principle of Material Frame Indifference, the free energy function $\bar{\Psi}^e_s$ is a function of the right elastic Cauchy–Green tensor $\overline{\boldsymbol{C}}^e$ via its invariants. Choosing the principal values of the right elastic Cauchy–Green tensor, $\overline{C}^e_A$, as a suitable set of invariants and noting that:

$$\overline{C}^e_A = \left(\lambda^e_A\right)^2 \qquad (\lambda^e_A = 1, 2, 3)$$

the hyperelastic formulation of Tamagnini et al. (2002) and Nova et al. (2003) can be extended to the finite deformation regime by replacing

the infinitesimal elastic strain invariants with the elastic logarithmic volumetric and deviatoric strains defined as follows:

$$\varepsilon_v^e := \hat{\varepsilon}_1^e + \hat{\varepsilon}_2^e + \hat{\varepsilon}_3^e \qquad \varepsilon_s^e = \sqrt{\frac{2}{3}\left\{(e_1^e)^2 + (e_2^e)^2 + (e_3^e)^2\right\}} \tag{14}$$

where $\hat{\varepsilon}_A^e = -\ln(\lambda_A^e)$ is the Ath elastic logarithmic principal strain and $e_A = \hat{\varepsilon}_A^e - \varepsilon_v^e/3$ its deviatoric part. The free energy function in the spatial setting then reads:

$$\hat{\psi}^e(\varepsilon_v^e, \varepsilon_s^e) = \tilde{\psi}(\varepsilon_v^e) + \frac{3}{2}\left\{G_0 + \frac{\alpha}{\hat{\kappa}}\tilde{\psi}(\varepsilon_v^e)\right\}(\varepsilon_s^e)^2 \tag{15}$$

where:

$$\tilde{\psi}(\varepsilon_v^e) := \begin{cases} \hat{\kappa} P_r \exp\left\{\left(\varepsilon_v^e/\hat{\kappa} - 1\right)\right\} & (\varepsilon_v^e \geq \hat{\kappa}) \\ P_r \varepsilon_v^e - P_r \left(\varepsilon_v^e - \hat{\kappa}\right)^2/(2\hat{\kappa}) & (\varepsilon_v^e < \hat{\kappa}) \end{cases} \tag{16}$$

In Eqs. (15) and (16), $\hat{\kappa}$, G_0 and α are material constants, whose physical meaning is discussed in Section 4, while P_r is a reference Kirchhoff mean stress, marking the transition from linear ($\varepsilon_v^e < \hat{\kappa}$) to non-linear ($\varepsilon_v^e \geq \hat{\kappa}$) elastic behavior.

A.2. Yield function and plastic potential

Due to the assumption of material isotropy, both the yield function and the plastic potential g depend on $\boldsymbol{\tau}$ through its invariants (P, Q, θ). The FD_Milan model adopts for the functions f and g the expressions provided by Lagioia et al. (1996) – transformed to the Kirchhoff stress space – for their flexibility in reproducing a wide range of experimental data:

$$f(P, Q, \theta, P_s, P_t) = P^* - A_f^{-K_{1f}/C_f} B_f^{K_{2f}/C_f} P_c^* = 0 \tag{17}$$

$$g(P, Q, \theta, P_t) = P^* - A_g^{-K_{1g}/C_g} B_g^{K_{2g}/C_g} \tilde{P}_c^* \tag{18}$$

where, for either $a = f$ or g:

$$K_{1a} := \frac{\mu_a(1-\alpha_a)}{2(1-\mu_a)}\left\{1 + \sqrt{1 - \frac{4\alpha_a(1-\mu_a)}{\mu_a(1-\alpha_a)^2}}\right\} \tag{19}$$

$$K_{2a} := \frac{\mu_a(1-\alpha_a)}{2(1-\mu_a)}\left\{1 - \sqrt{1 - \frac{4\alpha_a(1-\mu_a)}{\mu_a(1-\alpha_a)^2}}\right\} \tag{20}$$

$$A_a := 1 + \frac{1}{K_{1a} M_a(\theta)}\frac{Q}{P^*} \tag{21}$$

$$B_a := 1 + \frac{1}{K_{2a} M_a(\theta)}\frac{Q}{P^*} \tag{22}$$

$$C_a := (1-\mu_a)(K_{1a} - K_{2a}) \tag{23}$$

and:

$$P^* := P + P_t \qquad P_c^* := P_s + (1+k)P_t \qquad \tilde{P}_c^* := \tilde{P}_c + P_t \tag{24}$$

In the above equations, $\tilde{P}_c$ is a dummy parameter determined by setting $g = 0$ at the current state; the quantities α_f, μ_f, α_g and μ_g are material constants controlling the shape of the yield locus and of the plastic potential in the meridian plane ($Q : P$, at constant θ) of Kirchhoff stress space. The functions $M_a = M_a(\theta)$, appearing in Eqs. (21) and (22), control the shape of the yield surface and plastic potential in the deviatoric plane. In the model formulation, these functions are chosen in order to reproduce the regularized Mohr–Coulomb surface proposed by Abbo et al. (2011). Associative plastic flow is recovered when the constants α_g, μ_g and the function $M_g(\theta)$ are set equal to the corresponding quantities for the yield function f. A representation of the yield function in both $Q : P$ invariants plane and in principal Kirchhoff stress space is given in Fig. 1.

A.3. Hardening functions

The hardening functions for the internal variables P_s and P_t are given by:

$$h_s = \rho_s P_s\left(\hat{V} + \xi_s \hat{D}\right) \tag{25}$$

$$h_t = -\rho_t P_t\left(|\hat{V}| + \xi_m \hat{D}\right) \tag{26}$$

where:

$$\hat{V} := \mathrm{tr}\left(\frac{\partial g}{\partial \boldsymbol{\tau}}\right) \qquad \hat{D} := \sqrt{\frac{2}{3}}\left\|\mathrm{dev}\left(\frac{\partial g}{\partial \boldsymbol{\tau}}\right)\right\| \tag{27}$$

are the first and second invariants of the plastic potential gradient tensor. For $\xi_s = 0$, the preconsolidation stress undergoes purely volumetric hardening, and the material response is characterized by the existence of a Critical State locus in stress space. Eq. (27) describes the debonding process with a monotonic decrease of the bond strength P_t with accumulated volumetric and distortional plastic deformations.

Following Monforte et al. (2019), the evolution Eq. (7) can be recast in the alternative, integrated form:

$$P_s = P_{s0} \exp\left\{\rho_s\left(E_v^p + \xi_s E_s^p\right)\right\} \tag{28}$$

$$P_t = P_{t0} \exp\left\{-\rho_t\left(N_v^p + \xi_t E_s^p\right)\right\} \tag{29}$$

where E_v^p, E_s^p and N_s^p are three alternative (strain-like) internal variables, representing, respectively, the accumulated plastic volumetric deformation, the accumulated plastic deviatoric deformation and the accumulated norm of the plastic volumetric deformation. Their evolution equations are simply provided by:

$$\dot{E}_v^p = \dot{\gamma}\hat{V} \qquad \dot{E}_s^p = \dot{\gamma}\hat{D} \qquad \dot{N}_v^p = \dot{\gamma}|\hat{V}| \tag{30}$$

Eqs. (28) and (29) allow to determine the preconsolidation stress P_s and the bond strength P_t each material point and at each time t once the time evolution of the strain-like internal variables is known.

Appendix B. Extension of the FD_Milan model to non-local plasticity

The extension to non-local plasticity of the FD_Milan model is obtained by transforming the strain-like internal variables E_v^p, E_s^p and N_v^p to spatially averaged quantities in the neighborhood Ω of a material point $\boldsymbol{x} = \boldsymbol{\phi}(\boldsymbol{X}, t)$ at time t. In the numerical implementation of the model, the averaged values are computed by the following expressions:

$$\overline{E}_v^p(\boldsymbol{x}_i) = \frac{1}{\sum_{\boldsymbol{x}_j \in \Omega} w(\boldsymbol{x}_i, r_{ij})} \sum_{\boldsymbol{x}_j \in \Omega} w(\boldsymbol{x}_i, r_{ij}) E_v^p(\boldsymbol{x}_j) \tag{31}$$

$$\overline{E}_s^p(\boldsymbol{x}_i) = \frac{1}{\sum_{\boldsymbol{x}_j \in \Omega} w(\boldsymbol{x}_i, r_{ij})} \sum_{\boldsymbol{x}_j \in \Omega} w(\boldsymbol{x}_i, r_{ij}) E_s^p(\boldsymbol{x}_j) \tag{32}$$

$$\overline{N}_v^p(\boldsymbol{x}_i) = \frac{1}{\sum_{\boldsymbol{x}_j \in \Omega} w(\boldsymbol{x}_i, r_{ij})} \sum_{\boldsymbol{x}_j \in \Omega} w(\boldsymbol{x}_i, r_{ij}) N_v^p(\boldsymbol{x}_j) \tag{33}$$

where $r_{ij} = \left\|\boldsymbol{x}_j - \boldsymbol{x}_i\right\|$ is the distance between points located at $\boldsymbol{x}_j$ and $\boldsymbol{x}_i$, and w is a suitable weighting function, for which the expression proposed by Galavi and Schweiger (2010):

$$w(\boldsymbol{x}, r_{ij}) = \frac{r_{ij}}{\ell_c} \exp\left\{-\left(\frac{r_{ij}}{\ell_c}\right)^2\right\} \tag{34}$$

is adopted. The scalar quantity ℓ_c appearing in Eq. (34) (characteristic length) is a material constant providing the length scale necessary to render the numerical solution objective in presence of shear localization. Once the non-local quantities $\overline{E}_v^p$, $\overline{E}_s^p$ and $\overline{N}_v^p$ are known, the stress-like internal variables P_s and P_t are computed by Eqs. (28) and (29).

Appendix C. Supplementary data

Supplementary material related to this article can be found online at https://doi.org/10.1016/j.compgeo.2024.106343.

References

Abbo, A.J., Lyamin, A.V., Sloan, S.W., Hambleton, J.P., 2011. A C2 continuous approximation to the Mohr–Coulomb yield surface. Int. J. Solids Struct. 48 (21), 3001–3010.

Abe, K., Soga, K., Bandara, S., 2014. Material point method for coupled hydromechanical problems. J. Geotech. Geoenv. Engng. ASCE 140 (3), 04013033.

Adachi, T., Oka, F., Hirata, T., Hashimoto, T., Nagaya, J., Mimura, M., Pradhan, T.B.S., 1995. Stress–strain behavior and yielding characteristics of eastern Osaka clay. Soils Found. 35 (3), 1–13.

An, Y., Wu, Q., Shi, C., Liu, Q., 2016. Three–dimensional smoothed–particle hydrodynamics simulation of deformation characteristics in slope failure. Géotechnique 66 (8), 670–680.

Armero, F., Callari, C., 1999. An analysis of strong discontinuities in a saturated poro–plastic solid. Int. J. Numer. Methods Engng. 46 (10), 1673–1698.

Baligh, M.M., 1985. Strain path method. J. Geotech. Engng. ASCE 111 (9), 1108–1136.

Bažant, Z.P., Belytschko, T.B., Chang, T.-P., et al., 1984. Continuum theory for strain–softening. J. Engng. Mech. ASCE 110 (12), 1666–1692.

Bažant, Z.P., Jirásek, M., 2002. Nonlocal integral formulations of plasticity and damage: survey of progress. J. Engng. Mech. ASCE 128 (11), 1119–1149.

Bažant, Z.P., Lin, F.-B., 1988. Non–local yield limit degradation. Int. J. Numer. Methods Engng. 26 (8), 1805–1823.

Bažant, Z.P., Pijaudier-Cabot, G., 1988. Nonlocal continuum damage, localization instability and convergence. J. Appl. Mech. ASME 55, 287–293.

Beuth, L., Vermeer, P.A., 2013. Large deformation analysis of cone penetration testing in undrained clay. In: Installation Effects in Geotechnical Engineering. Taylor & Francis Group London.

Bisht, V., Salgado, R., 2018. Local transmitting boundaries for the generalized interpolation material point method. Int. J. Numer. Methods Engng. 114 (11), 1228–1244.

Borja, R.I., 2004. Computational modeling of deformation bands in granular media. II: Numerical simulations. Comput. Methods Appl. Mech. Engng. 193 (27–29), 2699–2718.

Borja, R.I., 2013. Plasticity: Modeling & Computation. Springer Science & Business.

Borja, R.I., Aydin, A., 2004. Computational modeling of deformation bands in granular media. I: Geological and mathematical framework. Comput. Methods Appl. Mech. Engng. 193 (27–29), 2667–2698.

Borja, R.I., Song, X., Rechenmacher, A.L., Abedi, S., Wu, W., 2013. Shear band in sand with spatially varying density. J. Mech. Phys. Solids 61 (1), 219–234.

Boschi, K., Arroyo, M., Monforte, L., Carbonell, J.M., Gens, A., 2024. Coupled hydromechanical modelling of cone penetration in layered liquefiable soils. Géotechnique 1–15.

Bui, H.H., Fukagawa, R., Sako, K., Ohno, S., 2008. Lagrangian meshfree particles method (SPH) for large deformation and failure flows of geomaterial using elastic–plastic soil constitutive model. Int. J. Numer. Anal. Methods Geomech. 32 (12), 1537–1570.

Burland, J.B., 1990. On the compressibility and shear strength of natural clays. Géotechnique 40 (3), 329–378.

Carbonell, J.M., Monforte, L., Ciantia, M.O., Arroyo, M., Gens, A., 2022. Geotechnical particle finite element method for modeling of soil-structure interaction under large deformation conditions. J. Rock Mech. Geotech. Engng. 14 (3), 967–983.

Carbonell, J.M., Oñate, E., Suárez, B., 2013. Modelling of tunnelling processes and rock cutting tool wear with the particle finite element method. Comput. Mech. 52 (3), 607–629.

Ceccato, F., Beuth, L., Vermeer, P.A., Simonini, P., 2016. Two-phase material point method applied to the study of cone penetration. Comput. Geotech. 80, 440–452.

Ceccato, F., Simonini, P., 2017. Numerical study of partially drained penetration and pore pressure dissipation in piezocone test. Acta Geotech. 12 (1), 195–209.

Chambon, R., Caillerie, D., Matsuchima, T., 2001. Plastic continuum with microstructure, local second gradient theories for geomaterials: localization studies. Int. J. Solids Struct. 38 (46–47), 8503–8527.

Chambon, R., Caillerie, D., Tamagnini, C., 2004. A strain space gradient plasticity theory for finite strain. Comput. Methods Appl. Mech. Engng. 193 (27–29), 2797–2826.

Ciantia, M.O., Oliynyk, K., Tamagnini, C., 2022. Finite deformation modelling of cone penetration tests in saturated structured clays. In: International Conference of the International Association for Computer Methods and Advances in Geomechanics. Springer, pp. 195–202.

de Borst, R., 1989. Numerical methods for bifurcation analysis in geomechanics. Ing.–Arch. 59 (2), 160–174.

de Borst, R., Mühlhaus, H.-B., 1992. Gradient–dependent plasticity: formulation and algorithmic aspects. Int. J. Numer. Methods Engng. 35 (3), 521–539.

Dohrmann, C.R., Bochev, P.B., 2004. A stabilized finite element method for the Stokes problem based on polynomial pressure projections. Int. J. Numer. Methods Fluids 46 (2), 183–201.

Galavi, V., Schweiger, H.F., 2010. Nonlocal multilaminate model for strain softening analysis. Int. J. Geomech. ASCE 10 (1), 30–44.

Hauser, L., Schweiger, H.F., 2021. Numerical study on undrained cone penetration in structured soil using G-PFEM. Comput. Geotech. 133, 104061.

Lagioia, R., Puzrin, A.M., Potts, D.M., 1996. A new versatile expression for yield and plastic potential surfaces. Comput. Geotech. 19, 171–191.

Leroueil, S., Vaughan, P., 1990. The general and congruent effects of structure in natural soils and weak rocks. Géotechnique 40 (3), 467–488.

Martinelli, M., Galavi, V., 2021. Investigation of the material point method in the simulation of cone penetration tests in dry sand. Comput. Geotech. 130.

Martinelli, M., Pisanò, F., 2022. Relating cone penetration resistance to sand state using the material point method. Géotech. Lett. 12 (2), 131–138.

Mataix Ferrándiz, V., Bucher, P., Rossi, R., Cotela, J., Carbonell, J.M., Zorrilla, R., Celigueta, M.A., Casas, G., Tosi, R., 2020. Kratos multiphysics (version 8.1). https://doi.org/10.5281/zenodo.3234644.

Mayne, P.W., 1991. Determination of OCR in clays by piezocone tests using cavity expansion and critical state concepts. Soils Found. 31 (2), 65–76.

Mayne, P.W., 2005. Integrated ground behavior: in–situ and lab tests. In: Deformation Characteristics of Geomaterials. Vol. 2, Taylor & Francis London, pp. 155–177.

Mayne, P.W., Agaiby, S.S., 2019. Profiling yield stress and identification of soft organic clays using piezocone tests. In: Proc., 16th Pan American Conf. on Soil Mechanics and Geotechnical Engineering, (Geotechnical Engineering in the XXI Century, Mexican Society of Geotechnical Engineering Cancun). pp. 220–227.

Mayne, P.W., Coop, M.R., Springman, S.M., Huang, A.-B., Zornberg, J.G., 2009. Geomaterial behavior and testing. In: Proceedings of the 17th International Conference on Soil Mechanics and Geotechnical Engineering. IOS Press, pp. 2777–2872.

Monforte, L., Arroyo, M., Carbonell, J.M., Gens, A., 2017a. G–PFEM: A particle finite element method platform for geotechnical applications. In: ALERT Geomaterials Workshop.

Monforte, L., Arroyo, M., Carbonell, J.M., Gens, A., 2018a. Coupled effective stress analysis of insertion problems in geotechnics with the particle finite element method. Comput. Geotech. 101, 114–129.

Monforte, L., Arroyo, M., Gens, A., Carbonell, J.M., 2018b. Hydraulic conductivity from piezocone on-the-fly: a numerical evaluation. Géotech. Lett. 8 (4), 268–277.

Monforte, L., Carbonell, J.M., Arroyo, M., Gens, A., 2017b. Performance of mixed formulations for the particle finite element method in soil mechanics problems. Comput. Part. Mech. 4 (3), 269–284.

Monforte, L., Ciantia, M.O., Carbonell, J.M., Arroyo, M., Gens, A., 2019. A stable mesh–independent approach for numerical modelling of structured soils at large strains. Comput. Geotech. 116, 103215.

Monforte, L., Gens, A., Arroyo, M., Mánica, M., Carbonell, J.M., 2021. Analysis of cone penetration in brittle liquefiable soils. Comput. Geotech. 134, 104123.

Moshfeghi, S., Taiebat, M., Lizcano, A., 2024. Validating the use of material point method and SANISAND model for relating the state parameter with cone tip resistance. In: Geo-Congress 2024. pp. 172–180.

Nova, R., Castellanza, R., Tamagnini, C., 2003. A constitutive model for bonded geomaterials subject to mechanical and/or chemical degradation. Int. J. Numer. Anal. Methods Geomech. 27 (9), 705–732.

Oliver, J., Cante, J.C., Weyler, R., González, C., Hernández, J., 2007. Particle finite element methods in solid mechanics problems. Comput. Methods Appl. Sci. 7, 87–103.

Oliynyk, K., Ciantia, M.O., Tamagnini, C., 2021. A finite deformation multiplicative plasticity model with non–local hardening for bonded geomaterials. Comput. Geotech. 137, Article no. 104209.

Oliynyk, K., Ciantia, M.O., Tamagnini, C., 2022. PFEM modeling of strain localization processes in non–local multiplicative plasticity. In: International Conference of the International Association for Computer Methods and Advances in Geomechanics. Springer, pp. 118–125.

Oliynyk, K., Ciantia, M.O., Tamagnini, C., 2023. Effect of soil permeability on CPTu test results in structured clay soils. In: 8th CNRIG, Palermo. Springer, pp. 460–467.

Paniagua, P., Andó, E., Silva, M., Emdal, A., Nordal, S., Viggiani, G., 2013. Soil deformation around a penetrating cone in silt. Géotech. Lett. 3 (4), 185–191.

Pastor, M., Blanc, T., Haddad, B., Drempetic, V., Sanchez Morles, M., Dutto, P., Stickle, M.M., Mira, P., Fernández Merodo, J.A., 2015. Depth averaged models for fast landslide propagation: mathematical, rheological and numerical aspects. Arch. Comput. Methods Eng. 22 (1), 67–104.

Pastor, M., Blanc, T., Pastor, M.J., 2009. A depth-integrated viscoplastic model for dilatant saturated cohesive-frictional fluidized mixtures: application to fast catastrophic landslides. J. Non-Newton. Fluid Mech. 158 (1–3), 142–153.

Regueiro, R.A., Borja, R.I., 2001. Plane strain finite element analysis of pressure sensitive plasticity with strong discontinuity. Int. J. Solids Struct. 38 (21), 3647–3672.

Salgado, R., 2022. The Engineering of Foundations, Slopes and Retaining Structures. CRC Press.

Salgado, R., Mitchell, J.K., Jamiolkowski, M., 1997. Cavity expansion and penetration resistance in sand. J. Geotech. Geoenv. Engng. ASCE 123 (4), 344–354.

Salgado, R., Prezzi, M., 2007. Computation of cavity expansion pressure and penetration resistance in sands. Int. J. Geomech. ASCE 7 (4), 251–265.

Simo, J.C., Hughes, T.J.R., 1998. Computational Inelasticity, vol. 7, Springer Science & Business Media.
Suzuki, Y., Lehane, B.M., 2015. Analysis of CPT end resistance at variable penetration rates using the spherical cavity expansion method in normally consolidated soils. Comput. Geotech. 69, 141–152.
Tamagnini, C., Castellanza, R., Nova, R., 2002. A Generalized Backward Euler algorithm for the numerical integration of an isotropic hardening elastoplastic model for mechanical and chemical degradation of bonded geomaterials. Int. J. Numer. Anal. Methods Geomech. 26, 963–1004.
Tamagnini, C., Ciantia, M.O., 2016. Plasticity with generalized hardening: constitutive modeling and computational aspects. Acta Geotech. 11 (3), 595–623.
Teh, C.I., Houlsby, G.T., 1991. An analytical study of the cone penetration test in clay. Géotechnique 41 (1), 17–34.
Truty, A., Zimmermann, T., 2006. Stabilized mixed finite element formulations for materially nonlinear partially saturated two–phase media. Comput. Methods Appl. Mech. Engng. 195 (13–16), 1517–1546.
Vardoulakis, I., Aifantis, E.C., 1991. A gradient flow theory of plasticity for granular materials. Acta Mech. 87 (3), 197–217.
Vardoulakis, I., Sulem, J., 1995. Bifurcation Analysis in Geomechanics. CRC Press.
Wu, W., Bui, H.H., 2021. Point-based methods and their applications in geomechanics. Acta Geotech. 16 (8), 2313–2313.
Yost, K.M., Yerro, A., Green, R.A., Martin, E., Cooper, J., 2022. MPM modeling of cone penetrometer testing for multiple thin–layer effects in complex soil stratigraphy. J. Geotech. Geoenv. Engng. ASCE 148 (2), 04021189.
Zervos, A., Papanastasiou, P., Vardoulakis, I., 2001. A finite element displacement formulation for gradient elastoplasticity. Int. J. Numer. Methods Engng. 50 (6), 1369–1388.
Zhang, W., Zou, J.-Q., Zhang, X.-W., Yuan, W.-H., Wu, W., 2021. Interpretation of cone penetration test in clay with smoothed particle finite element method. Acta Geotech. 16 (8), 2593–2607.